IDO - 16648

MTR - ETR TECHNICAL BRANCHES QUARTERLY REPORT

April 1 - June 30, 1960

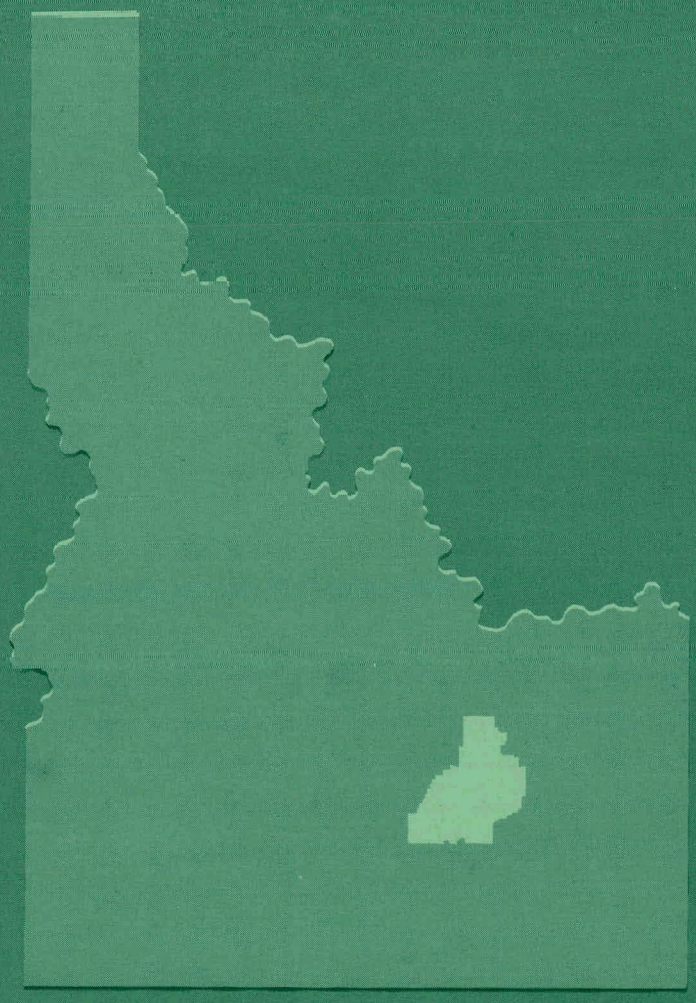

PHILLIPS PETROLEUM COMPANY

ATOMIC ENERGY DIVISION

NATIONAL REACTOR TESTING STATION

US ATOMIC ENERGY COMMISSION

DISCLAIMER

This report was prepared as an account of work sponsored by an agency of the United States Government. Neither the United States Government nor any agency Thereof, nor any of their employees, makes any warranty, express or implied, or assumes any legal liability or responsibility for the accuracy, completeness, or usefulness of any information, apparatus, product, or process disclosed, or represents that its use would not infringe privately owned rights. Reference herein to any specific commercial product, process, or service by trade name, trademark, manufacturer, or otherwise does not necessarily constitute or imply its endorsement, recommendation, or favoring by the United States Government or any agency thereof. The views and opinions of authors expressed herein do not necessarily state or reflect those of the United States Government or any agency thereof.

DISCLAIMER

Portions of this document may be illegible in electronic image products. Images are produced from the best available original document.

PRICE $2.00

Available from the
Office of Technical Services
U. S. Department of Commerce
Washington 25, D. C.

LEGAL NOTICE

This report was prepared as an account of Government sponsored work. Neither the United States, nor the Commission, nor any person acting on behalf of the Commission:

A. Makes any warranty or representation, express or implied, with respect to the accuracy, completeness, or usefulness of the information contained in this report, or that the use of any information, apparatus, method, or process disclosed in this report may not infringe privately owned rights; or

B. Assumes any liabilities with respect to the use of, or for damages resulting from the use of any information, apparatus, method, or process disclosed in this report.

As used in the above, "person acting on behalf of the Commission" includes any employee or contractor of the Commission, or employee of such contractor, to the extent that such employee or contractor of the Commission, or employee of such contractor prepares, disseminates, or provides access to, any information pursuant to his employment or contract with the Commission, or his employment with such contractor.

Printed in USA.

IDO-16648
AEC Research and Development Report
Reactor Technology
TID-4500 (16th Ed.)
Issued: January 25, 1961

MATERIALS TESTING REACTOR - ENGINEERING TEST REACTOR TECHNICAL BRANCHES QUARTERLY REPORT APRIL 1 - JUNE 30, 1960

J. R. Huffman
Assistant Manager, Technical

D. R. deBoisblanc
Director, Reactor Physics and Engineering

J. E. Evans
Director, Nuclear Physics

W. B. Lewis
Director, Theoretical Physics and Applied Mathematics

PHILLIPS
PETROLEUM
COMPANY

Atomic Energy Division
Contract AT(10-1)-205
Idaho Operations Office
U. S. ATOMIC ENERGY COMMISSION

Previous Quarterly Reports in the MTR-ETR Series

1958

Quarter	Number
1	IDO-16474
2	IDO-16481
3	IDO-16505
4	IDO-16532

1959

Quarter	Number
1	IDO-16543
2	IDO-16561
3	IDO-16580
4	IDO-16620

1960

Quarter	Number
1	IDO-16633

MTR-ETR TECHNICAL BRANCHES QUARTERLY REPORT

1960 QUARTER 2

APRIL 1 - JUNE 30, 1960

SUMMARY

Satisfactory operation of the ETR with the GEANP-99M7 experiment installed has been indicated with changes in loading and rod withdrawal sequence developed in the ETRC. The variation in other experimental fluxes in the ETRC due to withdrawal and insertion of the two GEANP experiments proposed during operation of the ETR are relatively small. Detailed horizontal neutron flux maps within the 400 g ETR fuel elements have established more accurate constants for extrapolating ETRC fluxes to "full power" ETR values and for determining heat transfer limitations. Comparison of a black and a gray absorber section on control rod No. 13 when partially inserted as a regulating rod shows at most only 7% more flux depression for the black section than for the gray. It has been shown that, for 400 g ETR fuel elements, 10% more boron in polyethylene tapes is required in order to be equivalent to boron uniformly distributed in the coolant space. Changing the metal-to-water ratio of the fuel elements in the ETR from 0.644 to 1.210 without a change in charge life is found to cause a 20% increase in thermal neutron flux in the inpile experiments for the 11% increase in U^{235} required.

The vertical thermal neutron flux distribution in each ETR fuel element was determined during Cycle 27 for the clean core and for the depleted core for use in experimental design and heat transfer calculations. Calculations have been made of the integrated power following a junior scram in the ETR for varying rod worths to determine the protection afforded by their use. Comparisons of calculated and measured thermal neutron fluxes in the ETRC have been made for variation in calculation techniques and reactor physics constants.

A procedure has been developed to investigate the nature of damage in the fuel element plates irradiated in the MTR by using electron microscopy of replicas of the surfaces after metallographic preparation. The full program of 14 capsules containing oxide fuel in the fuel element development program for the Experimental Gas Cooled Reactor is now installed in the ETR with the total burnup now ranging from 500 to 2500 Mwd/MT. Fundamental studies of the metal-water reaction of aluminum - 23.4 wt% uranium alloy indicate very low reaction rates up to 2300°F.

Calculations made to maximize the production of U^{233} + Pa^{233} from thorium slugs without exceeding a given heat generation rate indicate that the most efficient method is to use two different fluxes.

A preliminary measurement of the Co^{58} thermal cross section indicates that the 1500 b value makes a sizeable correction in the calculation of fast neutron fluxes from the threshold reaction $Ni^{58}(n,p)Co^{58}$. Preliminary total cross section data on Pa^{231} and Pu^{241} have been taken with the MTR chopper.

Crystal spectrometer measurements on the variation of eta for U^{233} in the region 0.01 to 1 ev have been compared with eta values obtained from MTR fission and total cross section data and with measurements made in other laboratories. Time-of-flight analyses of Bragg beams from Be crystal planes demonstrate the necessity of making such studies prefatory to high precision measurements. An investigation made into the system design of the MTR crystal spectrometer shielding cart drive to determine the system response to increasing the drive speed by a factor of 10 indicates that with appropriate design changes a stable system to meet the requirements can be obtained.

In the MTR nuclear chemistry program, results from triplicate analyses of the gas produced in highly irradiated Be are found to agree with yields of these gases calculated from cross sections and the neutron irradiation history. More accurate values for the half life of Cs^{134m} (2.90 ± 0.01 hr) and for its formation cross section (3.45 ± 0.2 b) have been obtained at the MTR. The activation yield ratios of metastable and ground states for Rh^{104} and Ir^{192} have been determined at thermal and at low energy resonances. Results giving comparisons among Au, Mn, and Na thermal and resonance flux monitors show good agreement. The activation thermal cross sections and resonance integrals for Pm^{147} going to the 5.3 d and 42 d Pm^{148} isomers, the pile cross sections of both isomers of Pm^{148}, the decay characteristic of 53 hr Pm^{149}, and gamma ray abundances for these activities have been measured.

In the inelastic scattering of slow neutrons program, energy and angular distribution measurements of slow neutrons scattered from methane have been compared with theoretical spectra and condensed to the "Scattering Law" presentation proposed by Egelstaff.

The decay of 15 d Eu^{156} has been studied to produce a level scheme for Gd^{156}. Recent measurements were made to determine the spins and parities of some of the previously reported energy levels using gamma-gamma directional correlation techniques.

The differential cross section of methane was calculated using the approximations of Krieger and Nelkin which greatly simplify the computations, and a method which is rigorous except for treating rotations classically. The two methods agree very well for neutron energies up to 0.1 ev, and give good overall agreement with data obtained on the MTR slow neutron velocity selector.

In IBM-650 program development a "650 Fortran Editor" program that operates on a machine without core storage or an on-line printer, and an analytical solution for a two-region, two-group treatment of an infinite one-dimensional configuration have been developed. The second program has been used for calculating the neutron multiplication in sandwiches of fuel elements, Cd, and moderator to develope safe storage and transportation assemblies.

MTR-ETR TECHNICAL BRANCHES QUARTERLY REPORT
1960 QUARTER 2
APRIL 1 - JUNE 30, 1960

CONTENTS

SUMMARY iii

I. OPERATIONS TECHNICAL SUPPORT 1

1. ETR CRITICAL FACILITY 1

1.1 ETRC Mockups of ETR Loading 1
1.2 Thermal Neutron Flux Distribution Within a 400-Gram Fuel Element 4
1.3 Thermal Neutron Flux Perturbations in ETR Due to Partial Insertion of Control Rod No. 13 . . 6
1.4 Reactivity Equivalence of Boron-Polyethylene Tapes and Boric Acid Solution 7
1.5 Effect of Increasing the Metal-Water Ratio of ETR Fuel Elements 9

2. THERMAL NEUTRON FLUX MEASUREMENTS IN ETR CYCLE 27 16

3. CALCULATION OF ETR JR. SCRAM ROD EFFECTS 17

4. MTR MAGNET GASKET MATERIAL TEST IN GAMMA RADIATION . . . 20

II. REACTOR PHYSICS AND ENGINEERING 21

1. COMPARISON OF TWO-DIMENSIONAL DIFFUSION THEORY CALCULATIONS WITH ETRC FLUX MEASUREMENTS 21

2. FUEL ELEMENT DEVELOPMENT 24

2.1 Sample Fuel Plate Fabrication 24
2.2 Sample Fuel Plate Irradiation and Testing 25
2.3 Development of Techniques for Electron Microscope Observation of the Nature of Damage in Fuel Plates 25

3. EGCR FUEL ELEMENT DEVELOPMENT 26

4. METAL-WATER REACTION PROGRAM 26

5. THORIUM PROGRAM 28

CONTENTS

6. NEUTRON FLUX MEASUREMENT TECHNIQUES 31

Co^{58} Thermal Neutron Cross Section 31

III. NUCLEAR PHYSICS 33

1. CROSS SECTIONS PROGRAM 33

1.1 Crystal Spectrometer Measurements of Eta for U^{233} . 33
1.2 Manganese Bath for Absolute Eta Measurements on U^{233} and Pu^{239} 34
1.3 Prompt Gamma-Rays from Fission of U^{233} 34
1.4 Coherent Inelastically Scattered Neutrons in Bragg Beams from a Be Crystal 34
1.5 Total Cross Section Measurements of Pa^{231} and Pu^{241} 36
1.6 Fission Cross Section of Pu^{241} 37
1.7 Fast Chopper Improvements 37

2. NUCLEAR CHEMISTRY 37

2.1 Beryllium Gases Experiment 37
2.2 Half-Life of Cs^{134m} and Cross Section for Its Formation by Neutron Activation 38
2.3 Yield Ratios of Isomeric Pairs by Neutron Activation 39
2.4 Neutron Flux Monitors 41
2.5 Alpha Experiment 42
2.6 Decay of 5.3-d Pm^{148} and 42-d Pm^{148} 43
2.7 Decay of Pm^{149} 44
2.8 Activation Cross Sections for Pm^{147} and the Pm^{148} Isomers 45

3. INELASTIC SCATTERING OF SLOW NEUTRONS PROGRAM 46

3.1 Scattering of Neutrons by Methane 46
3.2 The "Scattering Law" Presentation 47
3.3 Comparison of Experimental and Theoretical Scattered Neutron Spectra for Methane 51
3.4 Velocity Selector Modifications 52
3.5 Rotor Transmission Calculations 53
3.6 MTR Cold Neutron Facility 54

4. DECAY SCHEME STUDIES 56

The Decay of 15-Day Eu^{156} 56

5. EXPERIMENTAL TECHNIQUES AND INSTRUMENTATION 58

MTR Crystal Spectrometer Shielding Cart Drive Study . . . 58

CONTENTS

IV. THEORETICAL PHYSICS AND APPLIED MATHAMATICS 63

1. THEORETICAL WORK RELATED TO THE SLOW NEUTRON SCATTERING PROGRAM 63

1.1 Comparison of Procedures for Calculating Differential Cross Sections 63
1.2 Application of the Krieger-Nelkin Method to Calculation of $d\sigma/d\Omega$ and σ for CH_4 64
1.3 Average Values for Cosθ and Energy Transfer in CH_4 65

2. IBM-650 PROGRAM DEVELOPMENT 67

2.1 IBM-650 Fortran Editor Program 67
2.2 Sandwich Code 67

V. PUBLICATIONS OF MTR-ETR TECHNICAL BRANCHES 68

1. IDO REPORTS ISSUED 68

2. PAPERS PRESENTED AT MEETINGS 68

3. JOURNAL PUBLICATIONS 69

VI. REFERENCES 70

FIGURES

1. ETRC mockup of ETR cycle 26 loading gives average midplane thermal (2200 m/sec) neutron flux (10^{14} n/cm^2/sec extrapolated to 175 Mw. 2
2. ETRC mockup of 47-element loading with GEANP 9 x 9 loop gives average midplane thermal (2200 m/sec) neutron flux (10^{14} n/cm^2/sec) at 175 Mw. 3

FIGURES

3. ETRC mockup of 47-element loading shows neutron flux changes due to insertion and removal of GEANP fuel elements 4
4. Midplane thermal neutron flux distribution in the fuel region of an ETR fuel element with 400 g U^{235} in position N9 5
5. Midplane thermal neutron flux distribution in the fuel region of an ETR fuel element with 400 g U^{235} in position I-10 5
6. Vertical thermal neutron flux profile on north face of the PW fuel canister in position 66J13. 6
7. Vertical thermal neutron flux profile in position J11 6
8. Vertical thermal neutron flux profile in position H11 7
9. Reactivity comparison using rod no. 7 of boron impregnated polyethelene tapes and boric acid solution. 9
10. Comparison of average midplane thermal (2200 m/sec) neutron flux (10^{14} n/cm^2/sec) for M/W = 0.644 (middle number) . . . 10
11. Thermal neutron flux measurements in ETR cycle 27 in the clean core. 17
12. Thermal neutron flux measurements in ETR cycle 27 in the depleted core 17
13. Computing element interconnections to solve the differential equations for the ETR rod drop study 19
14. The calculated energy release from the ETR during rod drop as a function of rod worth 19
15. Experimental and calculated midplane thermal neutron (2200 m/sec) flux for cycle 27 (10^{14} n/cm^2/sec) normalized to 175 Mw. Calculations are based on a two-neutron energy group model with 4225 mesh points. . . . 22
16. Experimental and calculated midplane thermal neutron (2200 m/sec) flux for cycle 27 (10^{14} n/cm^2/sec) normalized to 175 Mw. Calculations are based on a two-neutron energy group model with 7387 mesh points. . . . 22
17. Experimental and calculated midplane thermal neutron (2200 m/sec) flux for cycle 26 (10^{14} n/cm^2/sec) normalized to 175 Mw. 23
18. Experimental and calculated thermal neutron (2200 m/sec) flux along the no. 10 row of cycle 26 normalized to 175 Mw. 23
19. Experimental and calculated thermal neutron (2200 m/sec) flux along the no. 9 row of cycle 27 (10^{14} n/cm^2/sec) normalized to 175 Mw. 24
20. Reaction rate of aluminum-23.4 wt% uranium alloy with water vapor at one atmosphere pressure as a function of temperature 27
21. Reaction rate of 99.99% purity aluminum with water vapor at one atmosphere pressure as a function of temperature . . 27
22. Eta for U^{233} from 0.02 to 1.0 ev. 33
23. Neutron counts vs flight time in μsec for the Be (103) beam at a Bragg angle of 23°22' 35

FIGURES

24. Total cross section of Pu^{239} from 0.02 to 0.125 ev 36
25. Total cross section of Pu^{241} from 0.02 to 0.20 ev 36
26. Time-of-flight spectrum of 0.07 ev neutrons scattered at an angle of 26° from methane at room temperature 47
27. The data of fig. 26 converted to: (a) a cross section in barns per angstrom steradian, and (b) barns per ev steradian. 48
28. Experimental cross sections for scattering of 0.025 ev neutrons. 49
29. Experimental cross section for scattering 0.07 ev neutrons. . 49
30. Experimental cross sections for scattering 0.10 ev neutrons . 50
31. The "Scattering Law" presentation of the methane data 50
32. The MTR cold neutron facility 54
33. Properties of Be filtered neutrons scattered by 1/16 in. vanadium sample. 55
34. Time spectra of beryllium filtered neutrons scattered by a 3/16 in. sample of vanadium 56
35. A level scheme for Gd^{156} incorporating results of new decay measurements. 58
36. Computing element interconnections to solve the differential equations for the MTR crystal spectrometer shielding cart drive study. 59
37. The coulomb friction torque of the MTR crystal spectrometer cart drive motor 61
38. The backlash in the gears of the MTR crystal spectrometer cart drive showing the dead zone, D. S. 61
39. Differential cross section for neutrons scattered from methane as a function of the scattering angle for various impact energies 64
40. Variation of the average cosine of the scattering angle with incident neutron energy for neutrons scattered by CH_4 . . . 65
41. Average energy transfer, $\overline{\epsilon}\ (\theta, E_o)$, as a function of the scattering angle for neutrons scattered by CH_4. 66
42. Mean energy transfer $\overline{\epsilon}\ (E_o)$ per collision as a function of the incident neutron energy for neutrons scattered by CH_4. 66

TABLES

1. Data on Boron-Impregnated Polyethylene Tape 8
2. Core Constants, Reactivity Measurements, and Results of Calculations for Three M/W Ratios in ETRC 12
3. ETRC Calculated Core Constants for Three M/W Ratios 14
4. Comparison of ETRC Midplane Thermal Neutron Flux in Experiments for M/W Ratios of 0.644 and 1.210 15
5. Measured Characteristics of Epoxy Resin with Gamma-Ray Radiation 20
6. Sample Fuel Plate Variables 24
7. Summary of Irradiated Thorium Slug Calculations 30
8. Comparison of Calculated and Measured Gas Contents of Neutron-Irradiated Beryllium from Tensile Strength Coupon . 38
9. Half-Life of Cs^{134m} 39
10. Neutron Activation Cross Section for Formation of Cs^{134m}. . . 40
11. Properties Assumed for Flux Monitors. 41
12. Thermal and Resonance Flux in VG-7. 42
13. Thermal Activation Cross Sections and Resonance Activation Integrals for Au, Mn, and Na. 42
14. Abundances of Beta and Gamma-Rays in 5.3-d Pm^{148}. 43
15. Abundances of Beta and Gamma-Rays in 42-d Pm^{148} 44
16. Activation Cross Sections of Pm^{147}. 45
17. Pile Activation Cross Sections of the Pm^{148} Isomers to 53-hr Pm^{149} 46
18. Experimental Coefficients of P Terms in γ - γ Angular Correlation Measurements and Spin Sequence Assignments. . . 57
19. Comparison of Calculated and Experimental Total Cross Sections per Hydrogen Atom in Methane 65

I. OPERATIONS TECHNICAL SUPPORT

1. ETR CRITICAL FACILITY

1.1 ETRC Mockups of ETR Loading

1.11 ETR Cycle 26 Loading (J. W. Hensheid, ETRC Staff) Early in 1960 (beginning with Cycle 26) the U^{235} contents of the fuel elements and control rod fuel sections in the ETR were increased to 400 g and 160 g respectively in order to lengthen the charge life. The control rod withdrawal sequence was also revised at this time in an attempt to maintain, as nearly as possible, the same relative flux distribution from the beginning to the end of the cycle. This rod withdrawal sequence is as follows:

(1)	1, 2, 3, 4	Black Rods
(2)	12	Gray Rods
(3)	10	
(4)	13	
(5)	5, 11, 15	
(6)	7, 9, 14	
(7)	6, 8, 16	

All inpile loops or their nuclear mockups were in place then, except for the GEANP-99M7 experiment facility. To minimize the effect which a later installation of this loop would have on the core thermal neutron flux distribution, two additional ETR fuel elements were placed in the 9 x 9 in. experimental space to approximate the effect of the GEANP test fuel element, with most of the remaining space being utilized for irradiation of loop surveillance capsules. The results of some of the measurements made in the ETRC on this loading have been reported previously [1]*. Fig. 1 is a core diagram showing the midplane thermal neutron (2200 m/sec) flux distribution. It should be noted that the actual loading for ETR Cycle 26 differed somewhat from the mockup. In the ETRC mockup, control rod No. 8 was withdrawn and No. 12 was inserted. At the request of GEANP, the withdrawal sequence of these two rods was reversed beginning with ETR Cycle 26. Also, the GEANP test fuel element, included in the ETRC mockup, was withdrawn from the Cycle 26 loading for ETR just prior to startup. (In general, these two differences tend to cancel one another with regard to the thermal neutron flux distribution.) Another minor difference is that the ETRC loading contained a mockup of the GEANP 33L10 loop, but in ETR, a 4-hole piece

*Numbers in brackets refer to entries in Section VI, References.

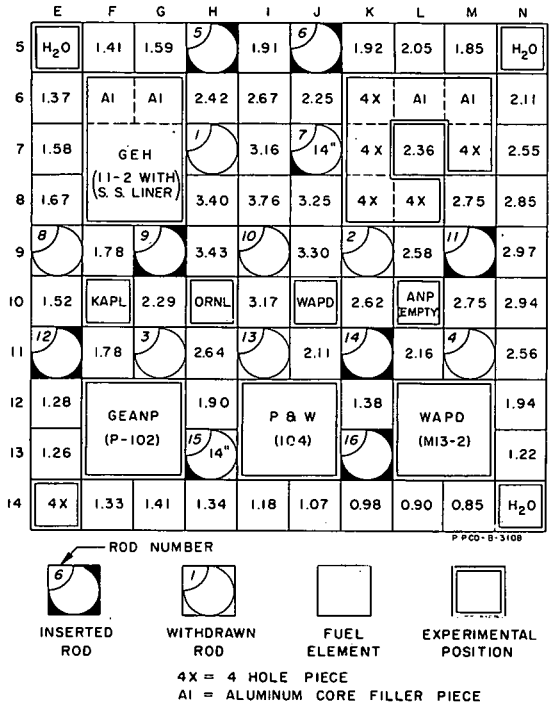

Fig. 1 ETRC Mockup of ETR Cycle 26 Loading gives average midplane thermal (2200 m/sec) neutron flux (10^{14} n/cm^2/sec) extrapolated to 175 Mw.

occupied this position during Cycle 26. The charge life of this loading is calculated to be 4400 MWD.

1.12 GEANP 99M7 Loop Installation (R. E. Oswald) In spite of the efforts mentioned in Section 1.11 to minimize the effect of the GEANP 99M7 loop installation, major core changes are necessary. All of the loop surveillance capsules presently located in the 99M7 facility are displaced when this loop is installed; therefore, in order to continue the irradiation program with these capsules, different core locations are required. GEANP also requested a change in the rod withdrawal program to minimize the variation of flux within the 99M7 loop during operation. Measurements have been made in the ETRC to establish a loading arrangement which fulfills both requirements and to evaluate the operating characteristics of the resulting loading.

Since variations in flux caused by withdrawing rods are greatest near the rod, one method of minimizing flux variations in the GEANP loops is to withdraw all rods adjacent to these loops prior to criticality. This can be accomplished by merely interchanging rods No. 5 and 7 in the rod withdrawal sequence. This change is not expected to increase appreciably the flux variations compared to those of the present rod withdrawal program.

The principle purpose of the loop surveillance program is the determination of the effects of fast neutron flux on materials used in loop construction. For the program to be of value it is necessary that these surveillance specimens receive an accumulated nvt greater than any loop does. Therefore, the core positions chosen, I8 and N10, are in the regions of highest flux (Fig. 1). Displacing elements in the high flux region to provide space for these capsules has the added advantage that it lowers the thermal neutron flux and consequently the heat flux in the hot-spot regions. In fact, as can be observed by comparing data in Fig. 1 and 2, the highest thermal neutron flux is actually lower in this loading, which contains only 47 elements, than it was in the Cycle 26 loading, which contained 51 elements.

Fig. 2 shows also the complete core loading and the control rod positions at criticality.

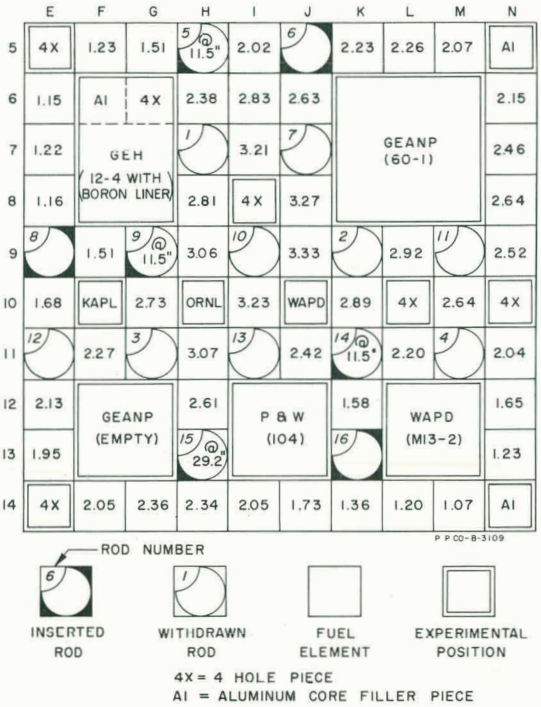

Fig. 2 ETRC Mockup of 47-element loading with GEANP 9 x 9 Loop gives average mid-plane thermal (2200 m/sec) neutron flux (10^{14} n/cm^2/sec) at 175 Mw. Fuel elements contain 400 g U^{235} and 2.16 g natural boron, and control rod fuel sections contain 160 g U^{235} and 0.71 g natural boron.

1.13 Thermal Neutron Flux Perturbations Caused by GEANP Experiments (R. E. Oswald) Operating procedures call for the test fuel elements in the two GEANP loops to be raised remotely into the core region after the ETR is at 100 Mw and in some cases after xenon equilibrium is reached. Later in the cycle it is also often the case that these test elements are remotely lowered from the core. It is important that other sponsors who have experiments in the reactor know what changes the insertion or removal of the GEANP elements cause to the thermal neutron flux in the regions where their experiments are located. These effects have now been measured in the ETRC.

It is almost certain that at one time or another during ETR operation only one of the two GEANP loops will contain a fuel element, while at other times either both loops, or neither, will contain a fuel element. Therefore the effects of three different changes have been determined: the insertion of a GEANP element in the 66G13 loop, the removal of the GEANP 99M7 element, and the combined effect of the two. The measurements were made in a mockup of the loading described in Section 1.12 with the reactivity changes compensated by equal displacements of rods No. 5, 9, and 14. This procedure duplicates the net change that would be experienced in the ETR since the reactor is critical on that set of rods in the rod withdrawal sequence.

The percentage changes in the thermal neutron flux throughout the core effected by the GEANP fuel element changes are shown in Fig. 3. It can be seen that the effect on the thermal neutron flux distribution of removing the GEANP 60-1 element from the 99M7 loop is relatively small. The reactivity effect of this change is approximately -0.2% $\Delta k/k$. The effect on the thermal neutron flux distribution of the insertion of the GEANP F-4 element in the 66G13 loop is also relatively small everywhere except in the immediate vicinity of the loop itself. The reactivity effect of this change is approximately +0.6% $\Delta k/k$. The greatest change to the thermal neutron flux occurs with the F-4 element in the 66G13 loop and the 99M7 loop empty, as shown in the diagram.

Static distributed poison techniques were used to balance rod worths and thus determine excess reactivity. The results are as

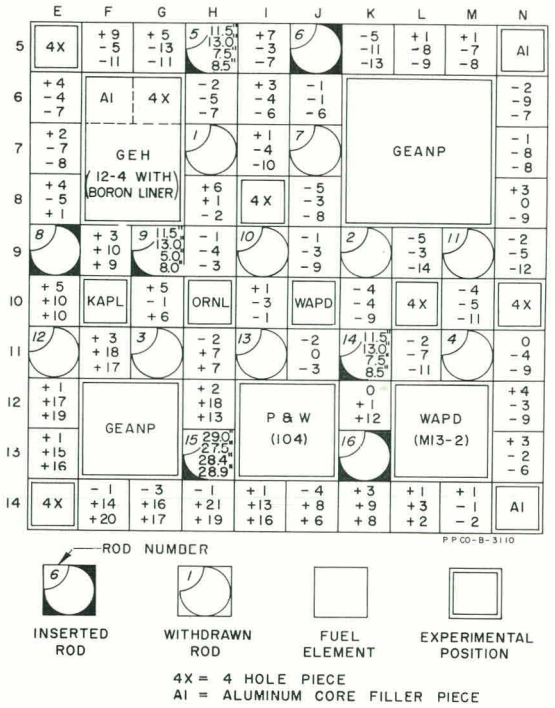

Fig. 3 ETRC Mockup of 47-element loading shows neutron flux changes due to insertion and removal of GEANP fuel elements. In each fuel element, the top number is the per cent change caused by removing GEANP 60-1 from 99M7; the middle number is the per cent change caused by insertion of GEANP F-4 in 66G13; and the bottom number is the per cent change caused by insertion of GEANP F-4 in 66G13 and removal of GEANP 60-1 from 99M7.

follows: (1) the combined worth of rods No. 5, 9, and 14 above the critical positions is 3.4% $\Delta k/k$, (2) the combined worth of rods No. 6, 8, and 16 is 3.1% $\Delta k/k$, and (3) these six rods give the total excess reactivity of 6.5% $\Delta k/k$.

It has been found that a loss in excess reactivity of nominally 1% $\Delta k/k$ occurs when a loading is transferred from the ETRC to the ETR. An additional reactivity loss due to the build-up of equilibrium xenon in the ETR (~ 4% $\Delta k/k$) occurs within 24 hr after startup. Thus, the available excess reactivity for the proposed loading is only 1.5% $\Delta k/k$ as compared with 4 to 7% $\Delta k/k$ for all previous 400 g ETR loadings. From an operational standpoint this means that the ability to override xenon after a spurious scram is considerably less than in past cycles. Therefore, although the thermal neutron flux distribution, the rod program, and the charge life (~ 2700 MWD) are satisfactory, the low xenon override potential will undoubtedly eliminate consideration of this loading for actual ETR operation. If the U^{235} content of the fuel elements were increased, so as to give greater excess reactivity, this loading would be quite satisfactory.

1.2 Thermal Neutron Flux Distribution Within a 400-Gram Fuel Element (A. D. Mackley, W. L. Schrader)

The thermal neutron (2200 m/sec) flux data from a large number of the flux runs reported by the ETRC group must be extrapolated to a core power of 175 MW for use in reactor calculations. An accurate extrapolation requires, of course, a complete knowledge of the flux distributions within the fueled regions of the core. Since it is impractical to obtain a complete knowledge of the flux in every core measurement, the flux usually is monitored only in a standard position (geometric center) in each fuel element. The thermal neutron absorption is much greater in the fueled region of a 400-g element than it is in the non-fueled regions adjacent to and between fuel elements, with the result that the flux at the center of the element is lower than the average flux within it. Extensive flux measurements have been made in order to

correlate the flux distribution within a fuel element with the flux at the standard position. Prior measurements having demonstrated that the vertical flux profile is essentially constant throughout the core, these studies were limited to the horizontal flux distribution.

Thirty gold foils on lucite wands were distributed approximately uniformly at the reactor midplane through the fueled region of each monitored element. Cadmium ratios were determined for each point separately and applied to the foil activation in the conventional manner to determine the thermal neutron flux for each point. Flux distributions within elements were measured in this manner in 11 different core positions which were considered representative of the core in general. Fig. 4 and 5 show two representative thermal neutron flux distributions observed at the midplane and demonstrate the existence of the expected thermal neutron flux gradients. It is convenient to define an "average-to-standard ratio" as the ratio of the average midplane thermal neutron flux to the thermal neutron flux at the standard position. The ratios measured in the 11 elements monitored range from 1.0 to 1.2 with a mean value of 1.13. Individual values depend upon the local core components. The 11 positions studied were so selected that their mean value should be representative of the mean value for all positions in the core. Therefore, the factor 1.13 is used in extrapolating flux data to higher power levels.

In order to determine the maximum heat flux in an element, it is also necessary to know the maximum thermal neutron flux within it. A measure of the thermal neutron flux peaking, which arises from the pronounced gradients, may be obtained by a comparison of the maximum midplane thermal neutron flux to the average midplane thermal neutron flux. The observed values for this "maximum-to-average ratio" range from 1.2 to 1.8 for the 11 elements monitored and have a mean value of 1.5. An effort was made to associate high and low values with particular regions of the core but no correlation was found.

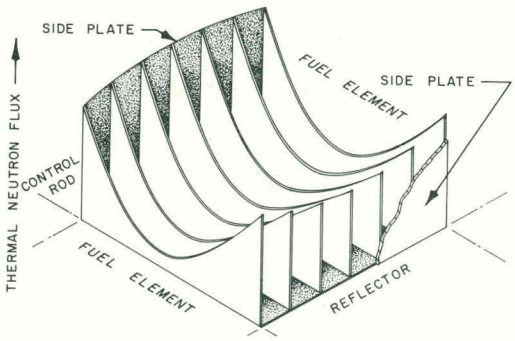

Fig. 4 Midplane thermal neutron flux distribution in the fuel region of an ETR fuel element with 400 g U^{235} in position N9.

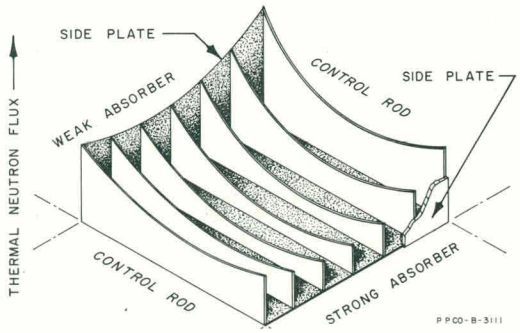

Fig. 5 Midplane thermal neutron flux distribution in the fuel region of an ETR fuel element with 400 g U^{235} in position I-10.

1.3 Thermal Neutron Flux Perturbations in ETR Due to Partial Insertion of Control Rod No. 13 (R. E. Oswald, J. W. Henscheid)

To allow more versatile operation of the ETR, it has been proposed to modify control rod No. 13 to permit it, as well as control rod No. 10, to be used as a regulating rod. The gray (nickel) absorber section of control rod No. 13 would be replaced with a black (boron-stainless steel) absorber to increase its worth closer to that of No. 10. In order to evaluate the effect which this change makes on the thermal neutron flux in adjacent experiments, three flux runs were made in the ETRC in a mockup loading of ETR Cycle 29. In the first run, shim rod No. 13, before modification, was fully withdrawn (36 in.). In the second run it was positioned at 29.5 in., the lower limit when operated as a regulating rod. In the third run the gray absorber section of the rod was replaced with a black absorber and the rod was again positioned at 29.5 in.

In each of the three runs, vertical thermal neutron flux profiles were measured at the center of fuel positions H11 and J11 and along the north face of the fuel canister in the PW loop (66 J13). These profiles are shown in Fig. 6, 7, and 8. The two columns on the right side of each figure give a point-by-point comparison of the perturbing effect of the partially inserted rod with black and with gray absorber

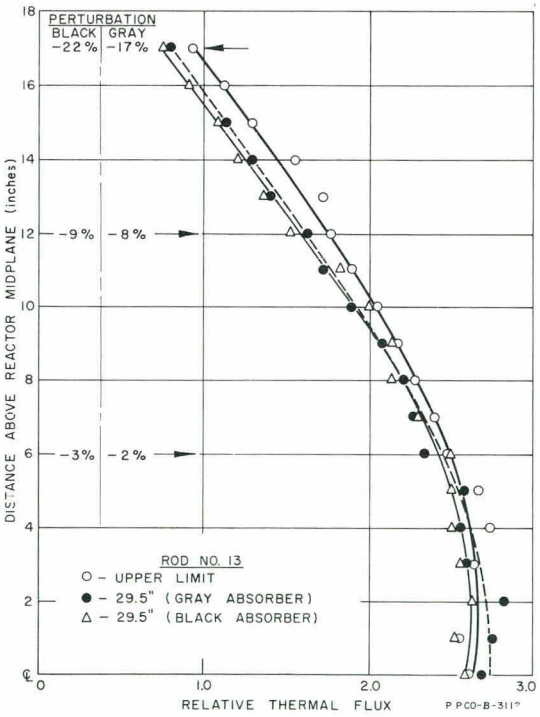

Fig. 6 Vertical thermal neutron flux profile on north face of the PW fuel canister in position 66J13. The two columns of figures list comparative perturbation effects of the rods inserted to 29.5 in.

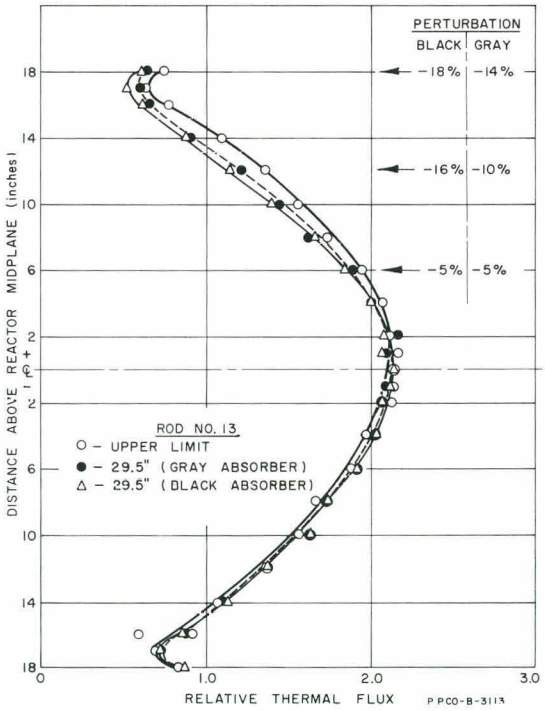

Fig. 7 Vertical thermal neutron flux profile in position J11. The two columns of figures list comparative perturbation effects of the rods inserted to 29.5 in.

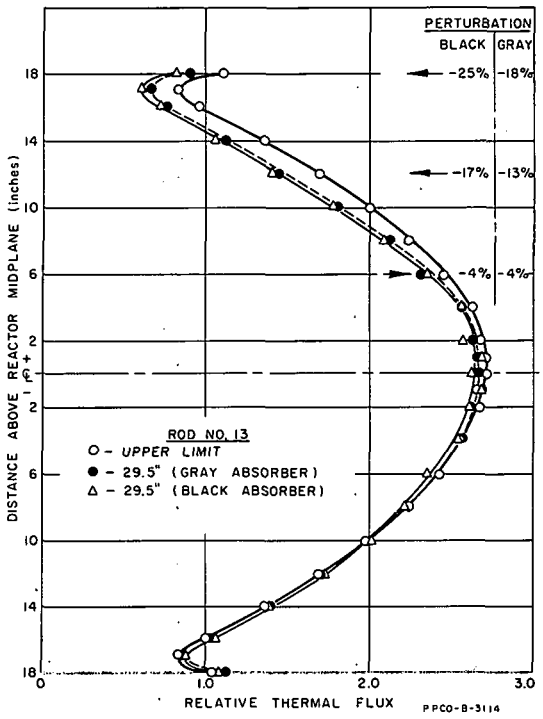

Fig. 8 Vertical thermal neutron flux profile in position H11. The two columns of figures list comparative perturbation effects of the rods inserted to 29.5 in.

sections. These data show that the black absorber section causes, at most, only 7% more flux depression than the gray absorber.

1.4 Reactivity Equivalence of Boron-Polyethylene Tapes and Boric Acid Solution (E. F. Aber)

Boron-impregnated polyethylene tapes and lucite wands are used at the ETRC to mock up reactivity effects, to uniformly poison the core, and as standards in the assaying of fuel assemblies for boron content. Both tapes and wands are cut to a length of 36 in. and are supported in the water channels of a fuel assembly by aluminum or plastic tabs at the top. Width, thickness, and boron content of tapes currently in use at the ETRC are given in Table 1.

From reactivity equivalence measurements made previously [2], it was concluded that, for the conditions of that experiment, boron-impregnated tape is equivalent to boron in solution. Since that time the fuel element U^{235} content has been increased from 256 to 400 g with a corresponding increase in flux peaking at the fuel element side plates (see Section 1.2). In most measurements in which boron tapes are used it is desirable that the boron occupy the same space as the fuel, or as an acceptable alternative occupy space which has an average flux equal to the average flux of the fuel region. Since the flux profile in an element is not flat, this condition may be hard to achieve. In order to evaluate the effects that could be expected when this condition is not achieved, it was decided to compare again the reactivity effect of the tapes with that of the boric acid solution and to check the effect of varying the distribution of tapes within an element.

For the reference standard, a stock solution of boric acid of known concentration was prepared and diluted to obtain various concentrations of boron. An unborated fuel element was made water-tight to contain the solution and a second unborated fuel element was used with the tapes. Reactivity measurements confirmed that these two elements have the same reactivity effects without boron added. The same core lattice position (J-11) was used for all measurements. Criticality runs were made with no boron, 1.5 g boron, and 3.0 g boron in the boric acid solution. The number of tapes of each type was adjusted to approximate these boron contents.

Table 1

DATA ON BORON-IMPREGNATED POLYETHYLENE TAPE

	Nominal weight-percent of boron							
	1 wt%		3 wt%		5 wt%		2 wt% (lucite)	
Width, in.	0.84		1.00		0.84		1.07	
Thickness, in.	0.019		0.018		0.018		0.064	
Boron per 36-in. tape, g	0.0868		0.253		0.396		0.222	
Standard deviation*(1), g	± 0.0059		± 0.0169		± 0.0077		---	
No. of tapes	36	18	12	6	8	4	14	7
Total boron, g	3.13	1.56	3.29	1.52	3.17	1.58	3.11	1.55
Standard deviation*(2), g	± 0.04	± 0.03	± 0.06	± 0.04	± 0.02	± 0.02	--	--

*Standard deviation of chemical analysis values.

(1) For one tape

(2) For the number of tapes listed

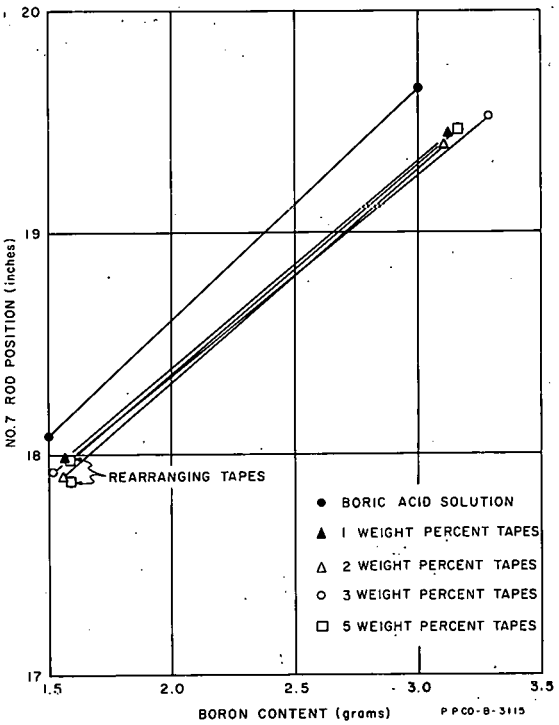

Fig. 9 Reactivity comparison using Rod No. 7 of boron impregnated polyethylene tapes and boric acid solution.

Fig. 9 shows No. 7 control rod position as a function of boron content in the fuel element; the reactivity change is linear with respect to rod position in this portion of the rod. The results show that a 10% greater amount of boron in the tapes is required to obtain the same reactivity effect as with boric acid solution. This indicates that self-shielding and perturbation effects of boron in the tapes are not negligible at boron concentrations of 1.5 to 3.0 g per fuel element volume. Positioning of tapes within the fuel element has an extreme effect equivalent to a 6% change in boron content. This effect is also shown in Fig. 9 for four 5-wt% tapes. The reactivity effect of the polyethylene in the tapes appears to be negligible, since a measurement made using a large number of unborated tapes shows no detectable effect.

The boron content of the polyethylene tapes was determined from chemical analyses of a number of samples of each type of tape. These results are shown in Table 1. The standard deviation of error associated with the total boron contained in several tapes (as used in these measurements) is smaller than that of an individual tape by a factor of $1/\sqrt{n}$ as shown in the table. The boron content of the lucite strips was determined from prior reactivity comparisons with polyethylene tapes in the ETRC, hence no error limits have been assigned. The error in the boric acid solution is estimated to be no more than ± 0.9% for the solution containing 3 g boron and ± 1.2% for the solution containing 1.5 g boron. These include weighing errors, volumetric errors, and errors due to impurities and water content in the H_3BO_3 crystals. The standard deviation of error associated with No. 7 rod positioning for criticality is ± 0.035 in.

1.5 Effect of Increasing the Metal-Water Ratio of ETR Fuel Elements (J. W. Henscheid)

At the request of Plant Engineering, nuclear measurements have been made on some effects of increasing the number of fuel plates in the ETR fuel element from 19 to 29. With no change in U^{235} content the increased metal-to-water volume ratio (1.210 compared to the present 0.644) would result in a decrease in the excess reactivity and charge life of the ETR core. Consequently, measurements were made in the ETRC to determine the increase in fuel content, which would give the same

charge life as the present ETR core gives. They included extensive thermal neutron flux measurements since a change in the neutron energy spectrum was anticipated.

Conclusions drawn from these measurements are:

(1) Changing the metal-water ratio of the fuel elements from 0.644 to 1.210 will require an 11% increase in U^{235} (445-g fuel elements and 180-g control rod fuel sections) to maintain the same charge life as the present ETR core has.

(2) Thermal neutron flux in most of the inpile experiments will increase approximately 20% due to the increased fast leakage.

1.51 Reactivity Measurements and Calculations Measurements were made in three separate runs in a mockup loading of ETR Cycle 27. In the first run 36 aluminum strips were inserted in each of the 51 fuel elements (two strips per water channel). The strips were 2S aluminum with nominal dimensions of 36 x 1 x 0.040 in. The metal-water ratio of these "loaded" fuel elements is 1.210. No change was made in the metal-water ratio of the control rod fuel sections, since the proposed redesign would change this ratio only very slightly. Critical rod positions were as shown in Fig. 10.

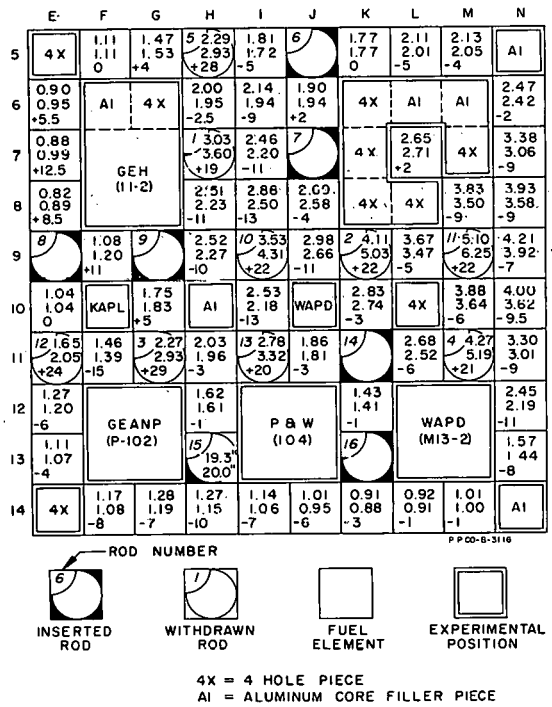

Fig. 10 Comparison of average midplane thermal (2200 m/sec) neutron flux (10^{14} n/cm^2/sec) for M/W = 0.644 (middle number). The bottom number shows the per cent change for increasing M/W from 0.644 to 1.210.

For the second run, one-half of the aluminum strips were removed from each fuel element (uniformly), giving a metal-water ratio of 0.927. Simultaneously, the core was uniformly poisoned with strips of boron-impregnated polyethylene tapes to compensate for the increase in reactivity due to the aluminum removal. Thus the critical rod positions for this run were essentially the same as for the first run.

A third run was made after removing all the remaining aluminum strips. The metal-water ratio is then that of a standard fuel element, 0.644. Additional uniform boron poisoning was inserted to compensate for the increase in reactivity and the critical rod positions were again the same.

The reactivity ρ, held down by the uniform boron poisoning

(equivalent to reactivity lost due to higher metal-water ratio), was calculated using the relationship

$$\rho \cong \frac{\Delta \Sigma_a}{\Sigma_a + \frac{1}{2} \Delta \Sigma_a} , \qquad (1)$$

where

$\Delta \Sigma_a$ is the macroscopic absorption cross section of the uniform boron poisoning homogenized over the core and

Σ_a is the total macroscopic absorption cross section of the core (homogenized) and includes fuel elements, control rod fuel sections, and gray absorber sections.

Some of the core constants used in these calculations are listed in Table 2 along with the calculated excess reactivities for the last two runs.

The increased fuel content required to compensate for the reactivity loss associated with an increase in metal-water ratio was calculated using the equation:

$$\rho = \frac{\Delta M}{M} (1-f) \qquad \text{or} \qquad \Delta M = \frac{\rho M}{(1-f)} \qquad (2)$$

where

M is the U^{235} fuel content of the core,

ρ is the reactivity loss (calculated by use of Eq. 1), and

f is the thermal utilization factor associated with a given metal-water ratio.

Table 2 shows the new fuel element and the control rod fuel section U^{235} content determined from this relationship. Inasmuch as the value of f is also increased, a recalculation of ΔM with a median value for f will give slightly higher U^{235} contents than shown in Table 2. For a metal-water ratio of 1.210, U^{235} contents for fuel elements and control rods are calculated to be about 480 and 195 g, respectively.

Study of the problem without benefit of experimental data reveals that the loss in reactivity, resulting from an increase in metal-water ratio, is due primarily to an increase in the fast leakage. Consider the three core loadings all identical except for their metal-water (M/W) ratios. Core 1 has M/W = 1.210 and $k_{eff} = 1$; Core 2 has M/W = 0.927 and $k_{eff} > 1$; Core 3 has M/W = 0.644 and $k_{eff} > 1$. The critical equation can be written:

$$k_{eff} = \eta \, \epsilon \, p \, f \, L_f \, L_t \quad , \text{ where}$$

Table 2

CORE CONSTANTS, REACTIVITY MEASUREMENTS, AND RESULTS OF CALCULATIONS FOR THREE M/W RATIOS IN ETRC

Core Constants	Run No. 1	Run No. 2	Run No. 3 (standard core)
Total U^{235}, g	22,000	22,000	22,000
M/W	1.210	0.927	0.644
Σ_a(fuel element), cm^{-1}	0.1623	0.1629	0.1634
Σ_a(fuel section), cm^{-1}	0.0756	0.0756	0.0756
Σ_a(gray section), cm^{-1}	0.1060	0.1060	0.1060
$^*\Sigma_a$(core), cm^{-1}	0.1445	0.1450	0.1454
Σ_a^{235}(core), cm^{-1}	0.1050	0.1050	0.1050
$\Delta\Sigma$(boron tapes), cm^{-1}	0	0.0040	0.0074
k_{ex}(boron tapes), % $\Delta k/k$	0	2.7	5.0
f(without boron tapes)	0.727	0.724	0.722
Loss in k_{ex}, % $\Delta k/k$	5.0	2.3	0
U^{235} increase to make up loss in k_{ex}, g	4030	1833	--
% increase in U^{235}	18.3	8.3	--
New fuel element mass, g	473	433	400
New fuel section mass, g	190	173	160
New Σ_a(core), cm^{-1}	0.1637	0.1537	--
New Σ_a^{235}(core), cm^{-1}	0.1242	0.1137	--
New f	0.759	0.740	--

$$^*\Sigma_a(\text{core}) = \frac{n(fe)\,\Sigma_a(fe) + n(fs)\,\Sigma_a(fs) + n(gs)\,\Sigma_a(gs)}{n(fe) + n(fs) + n(gs)}$$

where,

n(fe) is the number of fuel elements in the core,

n(fs) is the number of fuel sections (withdrawn rods), and

n(gs) is the number of gray sections (inserted rods).

η and the product ϵ p are assumed to be constant for all three cores, and

$$f = \frac{\Sigma_a(235)}{\Sigma_a(\text{total})} \qquad \text{(thermal utilization)}$$

$$L_t = \frac{1}{(1 + B^2 L^2)} \qquad \text{(thermal non-leakage probability)}$$

$$L_f = e^{-B^2\tau} \qquad \text{(fast non-leakage probability)}$$

These last three factors are evaluated in Table 3 using some conventional approximations. From this table it is apparent that the dominant factor in determining the change in k_{eff} is the fast non-leakage probability, L_f, with some effect being caused by the small change in f, i.e.,

$$k_{eff} = \text{constant} \times f\, L_f \,.$$

In Core 1, $k_{eff} = 1$, $f\, L_f = 0.565$, and constant = 1.77. The quantity k_{eff} can then be calculated for Cores 2 and 3 (Table 3). Although the values are somewhat larger than those found experimentally, the table does show that the effect is due almost entirely to the fast leakage, L_f, compared to changes that are noted in all other variables.

1.52 Flux Measurements During Runs 1 and 3, thermal neutron flux measurements were made to determine the change in the flux distribution in the experiments as well as in the fuel elements. The measurements were made using gold foils and bare and cadmium-covered gold wires. In general, the flux monitors were placed to provide a fairly complete flux map of the reactor midplane. In Run No. 1 the monitors were affixed to aluminum strips and in Run No. 3 to lucite wands. As expected, the cadmium ratio for gold decreased when the metal-water ratio was increased, the thermal fraction of the total foil activation decreasing approximately 10%. Prior measurements with bare and cadmium-covered uranium foils have shown that epithermal neutrons account for 11% of the total fission rate in a standard 400-g fuel element. For fuel elements with a metal-water ratio of 1.210 it is estimated that epithermal neutrons will account for 13% of the total fissions.

Fig. 10 also shows a comparison of the thermal flux maps made in Runs No. 1 and 3. In both cases the flux values were extrapolated to the operating power level of the ETR (175 Mw). On the average the thermal flux in the fuel elements decreased about 5% with the increase in metal-water ratio. This is due to the slightly higher epithermal fission rate and the 23% average increase in thermal flux in the control rod fuel sections.

Table 4 shows a comparison of the thermal fluxes measured in the experimental facilities for the two runs. The general and significantly higher fluxes in the core with the higher metal-water ratio are due to the increase in fast neutron leakage. This very fact accounts

Table 3

ETRC CALCULATED CORE CONSTANTS
FOR THREE M/W RATIOS

Constants	Core 1	Core 2	Core 3 (Standard Core)
M/W	1.21	0.927	0.644
Σ_a(total), cm^{-1}	0.1445	0.1450	0.1454
Σ_a(235), cm^{-1}	0.105	0.105	0.105
f	0.727	0.724	0.722
$\tau = 33 + 41.8$ M/W, cm^2	84	72	60
$D_f = 1.143 + 0.153$ M/W, cm	1.328	1.285	1.242
$L^2 = L^2_{H_2O}(1-f)$, cm^2	2.22	2.24	2.26
$D_t = L^2\Sigma_a$(total), cm	0.321	0.326	0.329
*B^2, cm^{-2}	0.003	0.003	0.003
$L_t = 1/(1 + B^2 L^2)$	0.994	0.994	0.994
$B^2\tau$	0.252	0.216	0.180
$L_f = e^{-B^2\tau}$	0.777	0.806	0.835
f x L_f	0.565	0.584	0.603
k_{eff} (calculated)	1.000	1.034	1.067
k_{eff} (experimental)	1.000	1.027	1.050

* Approximated using 30 x 30 x 36 in. parallelepiped.

Table 4

COMPARISON OF ETRC MIDPLANE THERMAL NEUTRON FLUX IN EXPERIMENTS FOR M/W RATIOS OF 0.644 AND 1.210

	Run 3 M/W = 0.644 (Standard Core)		Run 1 M/W = 1.210		Comparison of Runs 1 and 3	
Position*	Thermal Fraction	Thermal Flux, 10^{14} n/cm^{2}sec	Thermal Fraction	Thermal Flux, 10^{14} n/cm^{2}sec	Thermal Fraction, % change	Thermal Flux, % change
Average in Fuel Elements	0.534	2.07	0.479	1.97	-10%	-5%
Average in Control Rods	0.615	3.23	0.615	3.96	0	+23%
C-11	0.880	1.15	0.89	1.28	+1	+11
P-10	0.802	2.51	0.80	2.52	0	0
I-3	0.856	1.23	0.86	1.43	0	+16
I-16	0.758	0.61	0.76	0.70	0	+15
GEH-10 (33P7)	0.820	4.08	0.834	4.11	+1	+1
WAPD-M13-2						
T-3	0.583	1.39	0.611	1.72	+5	+24
T-6	0.628	1.32	0.618	1.47	-2	+11
P W (66J13)						
N	0.742	2.40	0.744	2.75	0	+15
S	0.749	1.68	0.744	1.96	-1	+17
WAPD-34 (J10)	0.286	0.55	0.310	0.69	+7	+25
KAPL (F-10)	0.502	1.10	0.507	1.21	+2	+10
GEANP (66G13)						
NE	0.359	0.53	0.329	0.54	-8	+2
SW	0.329	0.35	0.324	0.44	-2	+26
GEH 11-2 (69G7)						
SE	0.719	3.03	0.750	3.29	+4	+9
NW	0.726	2.17	0.735	2.70	+1	+24

* ETR Orientation

for the loss in excess reactivity when the metal-water ratio is increased. The small and inconsistent changes in thermal fractions (fraction of total activation of gold caused by thermal neutrons) shown in the table are within experimental error and are not considered to be particularly significant.

1.53 Conclusions One aspect of this metal-water ratio experiment which has not been taken into account is the increased importance of the withdrawn control rods in Run No. 1. It was pointed out earlier that the metal-water ratio in the proposed control rod fuel sections is practically the same as in the present fuel sections and that therefore no change was made in the metal-water ratio in the fuel sections during this experiment.

The midplane thermal neutron flux in the withdrawn control rods is, on the average, about 23% greater in Run No. 1 than in Run No. 3 (see Fig. 10 and Table 4). According to perturbation theory, control rod worths are roughly proportional to the square of the thermal neutron flux. One can then estimate that the rod worths for Run No. 1 are roughly 50% greater (i.e., $1.23^2 = 1.51$) than for Run No. 3. Experimental evidence to support this estimate is, unfortunately, rather meager. The worth of No. 15 rod, determined by period measurements, was found to be 0.37% $\Delta k/k$ in Run No. 3 and 0.49% $\Delta k/k$ in Run No. 1, or an increase of about 32% in rod worth.

In Run No. 3 (the so-called standard core) the excess reactivity held down by the inserted rods is about 7.6% $\Delta k/k$ plus the 5% $\Delta k/k$ held down by the boron tape poisoning, for a total of 12.6% $\Delta k/k$. Run No. 1 contained no boron poisoning but the inserted rods were identical to those in Run No. 3. On the basis of a conservative estimate that these rods, when withdrawn, will be 25% more effective than in Run No. 1, the excess reactivity would be 9.4% $\Delta k/k$. Thus the net loss in reactivity going from Run No. 3 to Run No. 1 would be the difference between only 12.6 and 9.5 or 3.1% $\Delta k/k$ rather than the 5% $\Delta k/k$ originally calculated. Using the same method as before to calculate the increased U^{235} mass to compensate for this loss, 445-g fuel elements and 180-g control rod fuel sections would be recommended.

Although the excess reactivity of the core with the new fuel elements would be the same as that for the present core, the charge life of the new core may be somewhat longer. This is due to the fact that the reactivity loss per megawatt-day will decrease when the total fuel mass in the core is increased. However, considering the small (11%) increase in fuel content and the approximate nature of the calculations, the error in assuming equal charge lives is probably small.

2. THERMAL NEUTRON FLUX MEASUREMENTS IN ETR CYCLE 27

Radiation Measurements Group

The vertical thermal neutron flux traverse in each fuel element of the ETR was determined with a clean core (0 MWD) and the depleted core

(4467 MWD) for Cycle 27 from the measured activities in irradiated 40-mil diameter cobalt wire. The measurements were at a reactor power of about 1 Mw, as calculated from coolant temperature and flowrate. The low power of values were extrapolated to the operating power of 175 Mw.

All Co^{60} activities were corrected for neutron flux depression and self-shielding effects by using the measured factor of 1.18. The Co^{59} cross section used in calculating the fluxes was 36.3 b. Corrections for the resonance contribution to the Co^{60} activity have also been made.

The maximum flux, the average flux, and the maximum-to-average ratio were calculated for each fuel element in the clean core (Fig. 11) and the depleted core (Fig. 12).

3. CALCULATION OF ETR JR. SCRAM ROD EFFECTS

S. R. Gossmann, K. V. Moore

Since control rod No. 13 is to be converted for possible regulating rod use (see Section 1.3), the Jr. scram rod may be either control

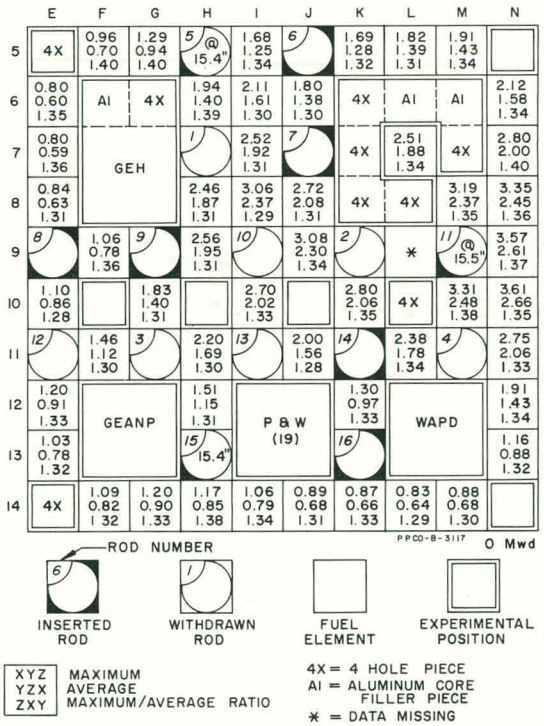

Fig. 11 Thermal neutron flux measurements in ETR Cycle 27 in the clean core showing maximum thermal neutron flux, average thermal neutron flux (10^{14} n/cm^2/sec), and the maximum-to-average ratio.

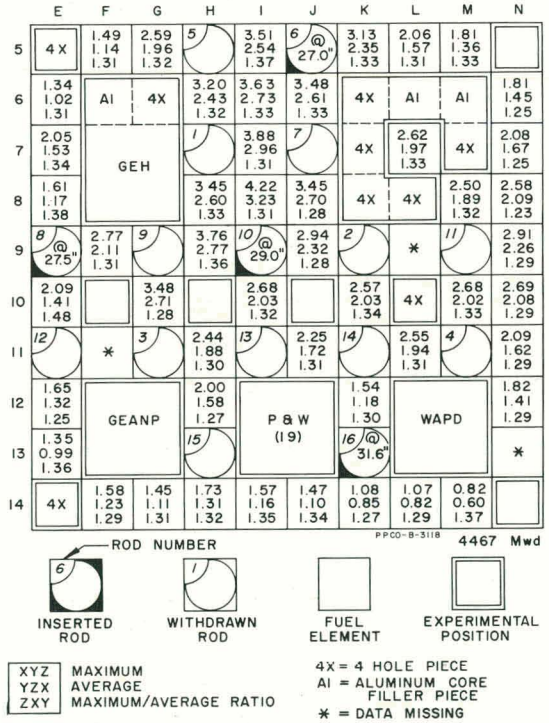

Fig. 12 Thermal neutron flux measurements in ETR Cycle 27 in the depleted core showing maximum thermal neutron flux, average thermal neutron flux (10^{14} n/cm^2/sec), and the maximum-to-average ratio.

rod No. 10 or No. 13 depending on which is not used in the servo control system. The two rods are not worth the same in reactivity (No. 13 is worth 3% $\Delta k/k$ and No. 10 is worth 2% $\Delta k/k$) thus requiring calculation of the integrated power following a Jr. scram for varying rod worths to determine the protection obtained by their use.

The differential equations describing the space independent time behavior of the reactor were solved by the Electronic Differential Analyzer (EDA). These are:

$$\frac{L}{\beta}\dot{N} + N = RN + \sum_{i=1}^{6} \frac{\beta_i}{\beta} D_i$$

$$\dot{D}_i + \lambda_i D_i = \lambda_i N \ , \ i = 1, 2, \ldots 6$$

where

$$N = \frac{n(t)}{n_o}$$

$$D_i = \frac{\psi_i(t)}{\psi_i(o)} = \frac{C_i(t)}{C_i(o)}$$

$$R = \frac{\rho(t)}{\beta} \quad \text{(dollars)}$$

and

L is the prompt neutron lifetime

β is the delayed neutron fraction from the emitters C_i

$n(t)$ is the neutron concentration or reactor power

n_o is neutron concentration at $t = 0$

$\rho(t)$ is the reactivity

D_i, $\psi_i(t)$ are auxilliary variables introduced for convenience in scaling

$C_i(t)$ is the concentration of the delayed neutron emitters of the ith group

and where the initial conditions are

$$N(0) = 1 \qquad D_i(0) = 1 \qquad R(0) = 0 \ .$$

Fig. 13 shows the interconnection of computing elements required

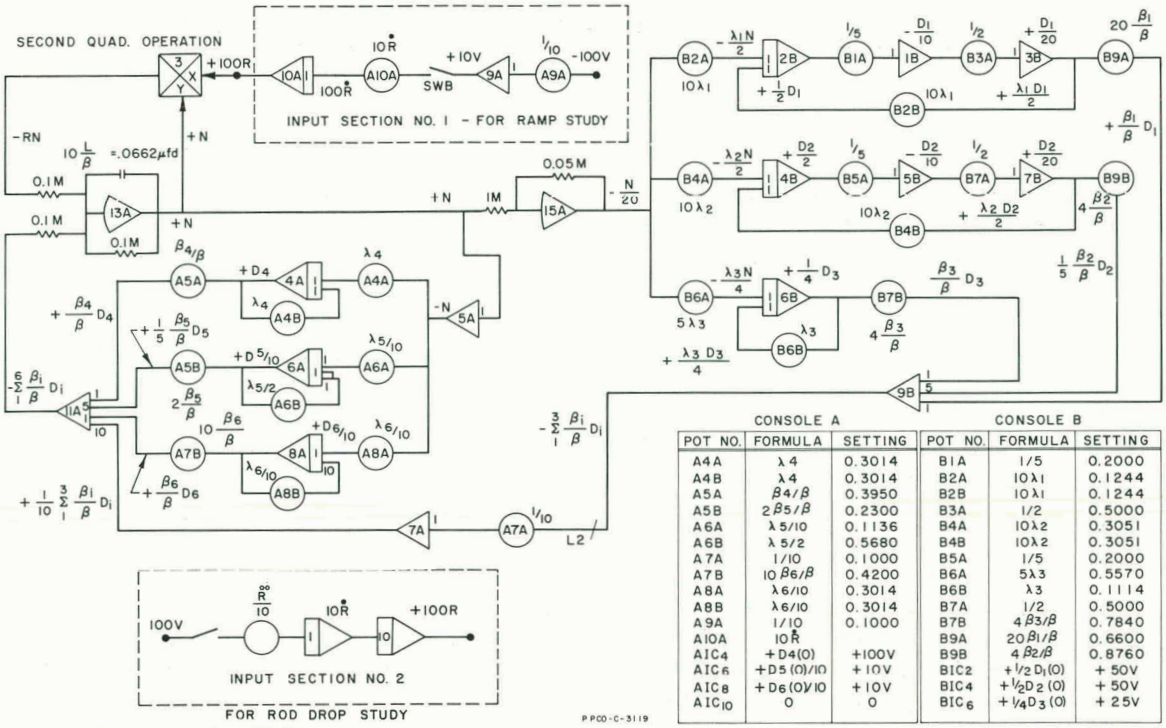

CONSOLE A			CONSOLE B		
POT NO.	FORMULA	SETTING	POT NO.	FORMULA	SETTING
A4A	$\lambda 4$	0.3014	B1A	1/5	0.2000
A4B	$\lambda 4$	0.3014	B2A	$10\lambda 1$	0.1244
A5A	$\beta 4/\beta$	0.3950	B2B	$10\lambda 1$	0.1244
A5B	$2\beta 5/\beta$	0.2300	B3A	1/2	0.5000
A6A	$\lambda 5/10$	0.1136	B4A	$10\lambda 2$	0.3051
A6B	$\lambda 5/2$	0.5680	B4B	$10\lambda 2$	0.3051
A7A	1/10	0.1000	B5A	1/5	0.2000
A7B	$10\beta 6/\beta$	0.4200	B6A	$5\lambda 3$	0.5570
A8A	$\lambda 6/10$	0.3014	B6B	$\lambda 3$	0.1114
A8B	$\lambda 6/10$	0.3014	B7A	1/2	0.5000
A9A	1/10	0.1000	B7B	$4\beta 3/\beta$	0.7840
A10A	$10\dot{R}$		B9A	$20\beta 1/\beta$	0.6600
AIC_4	$+D4(0)$	+100V	B9B	$4\beta 2/\beta$	0.8760
AIC_6	$+D5(0)/10$	+10V	BIC2	$+1/2\,D_1(0)$	+50V
AIC_8	$+D6(0)/10$	+10V	BIC4	$+1/2\,D_2(0)$	+50V
AIC_{10}	0	0	BIC_6	$+1/4\,D_3(0)$	+25V

Fig. 13 Computing element interconnections to solve the differential equations for the ETR rod drop study.

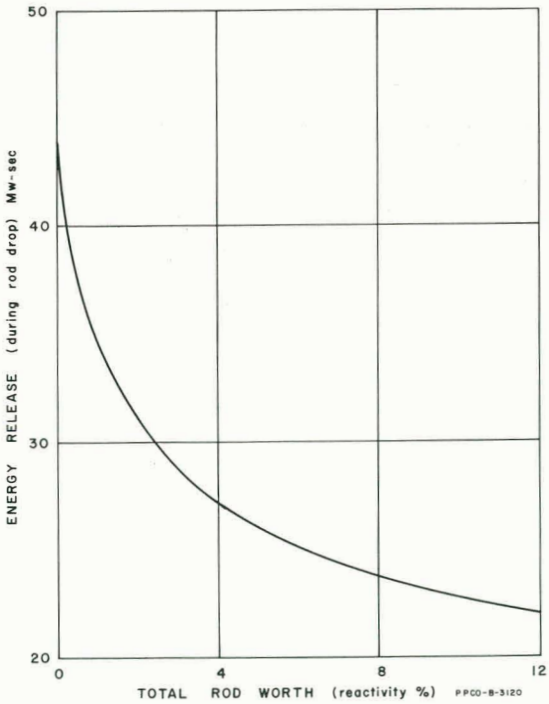

Fig. 14 The calculated energy release from the ETR during rod drop as a function of rod worth. Rod drop time is 0.25 sec for 3 ft drop. The acceleration is assumed to be 3 g and the power level at t = 0 is 175 Mw.

to solve these differential equations on the EDA. The rods are assumed to fall 3 ft with an acceleration of 3 g which correspond to a drop time of 0.25 sec. Because of the short drop time the problem was solved in "slow time", 10 times the actual time. However, the scaling is shown in "real time" in Fig. 13 for convenience. The rod worth is assumed to be a linear function of rod position.

The results of this study are given in Fig. 14, where the energy release during the rod drop vs the total rod worth is plotted. It is interesting to note the rather large decrease in this energy release at first with only 7% less energy release for rods worth 3% compared to those worth 2%.

4. MTR MAGNET GASKET MATERIAL TEST IN GAMMA RADIATION

B. G. Nelson

Measurements have been made on a number of materials which were considered for use as gaskets to seal the MTR magnets against water leakage in a high radiation field. Among those that were considered as possible materials for this application were the linear polyethylene materials and the epoxy resins.

Checks were made on some of the characteristics of a material with the trade name designation of "Epoxy 2662" as well as the same material loaded respectively with boron, lead, and iron. Spot checks of the characteristics of these materials are given in Table 5. In addition to these listed results there were no detectable changes in the physical sizes of the samples for a total radiation dosage of 3.6×10^8 R.

It should be noted that these checks are essentially for two points on a curve. For any broad usage of these materials in radiation fields a more comprehensive test of these characteristics should be made. The epoxy data are given here as a reference of a single check made on their radiation characteristics. Since the epoxy material has no apparent advantage over the linear polyethylene, the polyethylene has been chosen for the gasket material with good experimental results.

Table 5

MEASURED CHARACTERISTICS OF EPOXY RESIN WITH GAMMA-RAY RADIATION

Material	Gamma-ray Dosage, R	Hardness, Rockwell - R	Total Compression Load, lb
Epoxy 2662	0	119	10,000
Epoxy 2662	1.8×10^8	121	------
Epoxy 2662	3.6×10^8	121	5,900
Epoxy 2662/Boron	0	117	22,500
Epoxy 2662/Boron	1.8×10^8	120	------
Epoxy 2662/Boron	3.6×10^8	120	15,000
Epoxy 2662/Lead	0	112	17,500
Epoxy 2662/Lead	1.8×10^8	114	------
Epoxy 2662/Lead	3.6×10^8	113	6,800
Epoxy 2662/Iron	0	116	33,200
Epoxy 2662/Iron	1.8×10^8	125	------
Epoxy 2662/Iron	3.6×10^8	124	41,300

II. REACTOR PHYSICS AND ENGINEERING

1. COMPARISON OF TWO-DIMENSIONAL DIFFUSION THEORY CALCULATIONS WITH ETRC FLUX MEASUREMENTS

R. A. Grimesey, J. W. Henscheid

Additional comparisons of calculated and measured thermal neutron fluxes have been made for the ETRC mockups of Cycles 26 and 27 in the ETR [3]. Both measurements and calculations were made with a full complement of experiments in the core. Two- and four-group calculations were made with the two-dimensional IBM-704 Diffusion Code PDQ-03 [4], using X-Y geometry. The maximum number of mesh points available in the code is 7500 and the maximum number of nuclear compositions is 35. Both of these factors limit the amount of detail which can be included in the description of the core loadings.

Because the inpile tubes of the experiments are heavy absorbers of thermal neutrons, they were included as separate compositions and homogenized independently of the experiments. The experiments were homogenized over 36 in. vertically and over the approximate areas they occupy in the horizontal cross section of the core. The cylindrical inpile tubes and experimental regions were represented as squares of the approximate area they occupy in the core.

The fuel elements, shim fuel sections, and gray rod poison sections were homogenized as separate compositions because they have widely varying thermal properties. In the 7387 mesh point representations for Cycle 27 the aluminum side plates were included separately from the fuel plates in order to include the side plate peaking of thermal flux in the fuel elements. This effect also enables steeper thermal flux gradients across the fuel region and experiments to be obtained.

The thermal constants for the 35 compositions were averaged over a Maxwellian thermal spectrum at a temperature of 20°C. The fast group constants were obtained from Muft III [5] with a homogeneous fission spectrum for both the fuel regions and experiments. Thermal self-shielding factors were obtained from a double P-1 transport code [6] for the fuel elements, and the P-3 transport code [7] was coupled with the diffusion theory for the experiments. The accuracy of the self-shielding factors for the experiments is questionable because of the inherent limitations of the one-dimensional P-3 model for the very heterogeneous experiments.

The comparison of midplane thermal fluxes at 175 Mw with the ETRC measurements is given in Fig. 15 through 19. Fig. 15, 16, and 17 indicate the comparison of the calculated and measured thermal flux at

	E	F	G	H	I	J	K	L	M	N
5		0.94 1.10 +17	1.20 1.33 +10.8	5	1.51 1.66 +9.9	6	1.72 1.91 +12.2	1.97 2.09 +6.1	2.00 2.08 +4	
6	0.824 0.986 +19.4			1.78 1.95 +10	2.04 2.08 +1.96	1.83 2.05 +12.5				2.34 2.36 +.8
7	0.850 1.00 +17.6			1	2.42 2.44 +.7	7		2.38 2.88 +21		2.81 2.94 +4.6
8	0.814 0.980 +19.5			2.42 2.40 +.7	2.87 2.79 -2.8	2.58 2.70 +4.65			3.10 3.37 +8.7	3.35 3.21 -6
9	8	1.06 1.19 +12	9	2.49 2.45 -2	10	2.84 2.73 -3.8	2	2.90 3.19 +10	11	3.30 3.12 -5.5
10	0.956 1.05 +9.5		1.64 1.82 +11		2.50 2.44 -2.4		2.61 2.57 -1.5		3.11 3.15 +1.3	3.36 3.05 -10
11	12	1.30 1.38 +6.1	3	1.97 2.09 +6.1	13	1.83 1.85 +1.1	14	2.33 2.23 -4.3	4	2.98 2.52 -14
12	1.09 1.14 +4.6			1.42 1.61 +13.4			1.27 1.35 +5.5			2.18 1.81 -17
13	0.954 1.00 +5.2			15			16			1.44 1.23 -14.6
14		0.99 0.964 -2.6	1.08 1.05 -2.8	1.05 1.11 +5.7	1.00 1.13 +13	0.956 1.06 +10.5	0.902 0.94 +4.5	0.930 0.88 -5.4	1.02 0.892 -12.8	

PPCO-B-3121

TOP VALUE: ETRC MEASUREMENTS
CENTER VALUE: PDQ CALCULATIONS
BOTTOM VALUE: PERCENTAGE DIFFERENCE WITH EXPERIMENTAL VALUE AS BASE.

Fig. 15 Experimental and calculated mid-plane thermal neutron (2200 m/sec) flux for Cycle 27 (10^{14} n/cm^2/sec) normalized to 175 Mw. Calculations are based on a two-neutron energy group model with 4225 mesh points.

	E	F	G	H	I	J	K	L	M	N
5		0.94 1.10 +17	1.20 1.32 +10	5	1.51 1.65 +11.9	6	1.72 1.86 +9.3	1.97 2.04 +3.5	2.00 2.01 +.5	
6	0.824 0.988 +20			1.78 1.96 +10.1	2.04 2.09 +2.5	1.83 2.04 +11.5				2.34 2.28 -2.6
7	0.850 1.01 +19			1	2.42 2.43 +.4	7		2.38 2.71 +13.9		2.81 2.81 +0
8	0.814 0.992 +22			2.42 2.40 -.8	2.87 2.75 -4.2	2.58 2.65 +2.7			3.10 3.18 +2.6	3.35 3.07 -8.4
9	8	1.06 1.20 +13.2	9	2.49 2.42 -2.8	10	2.84 2.70 -4.9	2	2.90 2.96 +2.1	11	3.30 3.07 -7.0
10	0.956 1.12 +16.8		1.64 1.83 +11.5		2.50 2.43 -2.8		2.61 2.46 -5.75		3.11 2.98 -4.2	3.36 2.93 -13
11	12	1.30 1.47 +13	3	1.97 2.09 +6.1	13	1.83 1.83 +0	14	2.33 2.12 -9.0	4	2.93 2.45 -16.4
12	1.09 1.29 +18.3			1.42 1.65 +16.2			1.27 1.33 +4.7			2.18 1.76 -19.3
13	0.954 1.14 +18.8			15			16			1.44 1.21 -16
14		0.99 1.08 +9	1.08 1.15 +6	1.05 1.19 +13	1.00 1.18 +18	0.956 1.09 +13	0.902 0.964 +6.7	0.930 0.898 -3.3	1.02 0.894 -11	

PPCO D 3122

TOP VALUE: ETRC MEASUREMENTS
CENTER VALUE: PDQ CALCULATIONS
BOTTOM VALUE: PERCENTAGE DIFFERENCE WITH EXPERIMENTAL VALUE AS BASE.

Fig. 16 Experimental and calculated mid-plane thermal neutron (2200 m/sec) flux for Cycle 27 (10^{14} n/cm^2/sec) normalized to 175 Mw. Calculations are based on a two-neutron energy group model with 7387 mesh points.

the center of each fuel element over the core for Cycles 26 and 27. The comparison here is limited in that no measured thermal flux shapes across the fuel elements are available and steep thermal flux gradients are present. The measurements were made with a single foil in the center water channel of each fuel element.

Fig. 18 and 19 indicate the same comparison across the center of the 10 row and 9 row in Cycles 26 and 27, respectively. The 9 row of Cycle 27 contained only fuel elements and gray rods while the 10 row of Cycle 26 contains four experiments. Five foils in each fuel element were used in the measurements across the 9 and 10 row. The agreement across the 9 row of Cycle 27 is good in that the calculated thermal flux shape agrees in general with the measurements. However, it is seen that the flux gradients are not as steep in the calculations as indicated in the measurements. This is due to three factors:

(1) The homogenization scheme used.

(2) The numerical approximations to the derivatives used in the machine program.

(3) The inaccuracy of diffusion theory near internal boundaries.

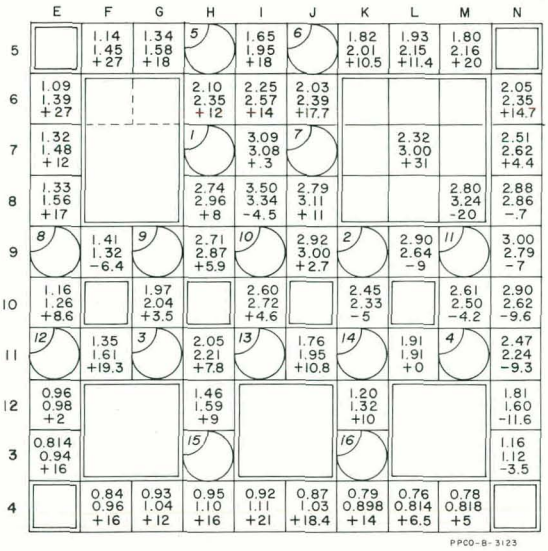

TOP VALUE: ETRC MEASUREMENTS
CENTER VALUE: PDQ CALCULATIONS
BOTTOM VALUE: PERCENTAGE DIFFERENCE WITH EXPERIMENTAL VALUE AS BASE.

Fig. 17 Experimental and calculated midplane thermal neutron (2200 m/sec) flux for Cycle 26 (10^{14} n/cm^2/sec) normalized to 175 Mw. Calculations are based on a two-neutron energy group model with 4225 mesh points.

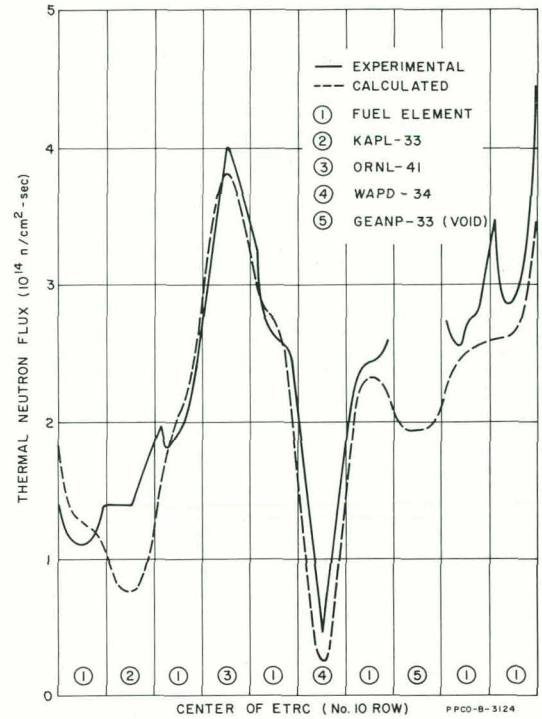

Fig. 18 Experimental and calculated thermal neutron (2200 m/sec) flux along the No. 10 row of Cycle 26 normalized to 175 Mw. Calculations are based on a two-neutron energy group model with 4225 mesh points.

The problems using the two- and four-energy groups with the 7387 mesh give a better fit than the two-energy group 4225 mesh. The machine time necessary for the fine mesh problems was about double that for the coarse mesh.

The 10 row of Cycle 26 indicates the comparison across typical experiments. The calculated flux across the KAPL-33 and WAPD-34 experiments is much lower than are the measured values. A number of factors which are being investigated at present can account for this. The use of the same fast and thermal neutron spectrums in the experiments that are characteristic of the fuel regions will generate lower thermal fluxes in the experiments than actually is the case. Both of these experiments are highly heterogeneous in the vertical dimension and the flux measurements were made only at the midplane. Since the contents of the experiments were homogenized in the vertical dimension for the calculations, the calculated fluxes were based on average nuclear properties while the measurements represent point values. This latter factor alone can account for wide discrepancies in the comparisons.

Further calculations are being carried on at present to obtain more realistic models for the generation of fast and thermal constants and self-shielding factors for the experiments in order to more

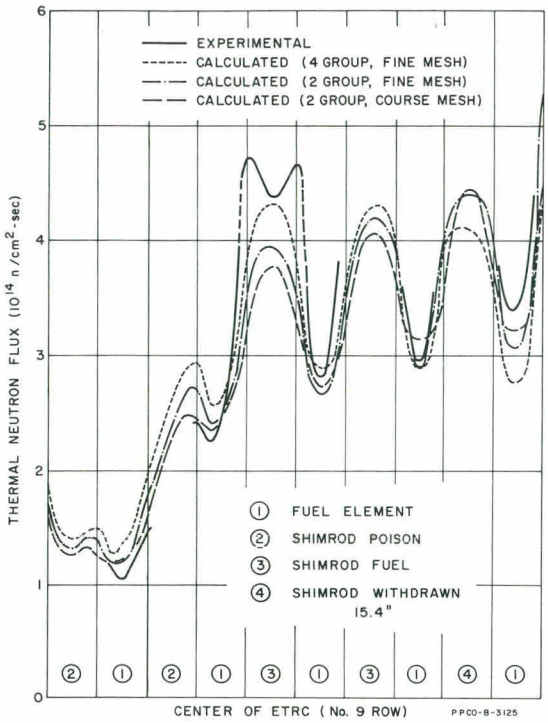

Fig. 19 Experimental and calculated thermal neutron (2200 m/sec) flux along the No. 9 row of Cycle 27 (10^{14} n/cm^2/sec) normalized to 175 Mw. Calculations were made with 7387 mesh points.

accurately calculate thermal flux in the ETR.

2. FUEL ELEMENT DEVELOPMENT

W. C. Francis

Work in Fuel Element Development during the second quarter has been devoted mainly to (1) fabrication of new fuel plates, involving as variables both fuel and cladding material for testing in the MTR, (2) continued irradiation of 22 fuel compositions in the L-51 position of the MTR, (3) preliminary hot cell examination of 10 compositions some of which have been irradiated to 70% burnup of the U^{235}, (4) development of techniques for electron microscope observation of the nature of damage in the plates, and (5) preparation of a report summarizing the progress of the program.

2.1 Sample Fuel Plate Fabrication (G. W. Gibson, B. G. Carlson)

The feasibility of fabricating fuel plate samples in the range of variables shown in Table 6 was investigated with satisfactory techniques being developed for all but the plates with very thin cladding.

Table 6

SAMPLE FUEL PLATE VARIABLES

Core Compositions		Cladding	
Material	Thickness (in.)	Material (Al)	Thickness (in.)
18 - 30 wt% U-Al Alloy	0.016 - 0.020	1100	0.006 - 0.015
		X 8001	
		X 8002	
		M 257	

The aluminum powder alloy M 257 with 5% Al_2O_3 was used as cladding material. This material has good corrosion resistance to deionized water and excellent high temperature mechanical properties. The difference in the properties of the M 257 alloy and the 1100 aluminum picture frames and cores caused the cores and picture frames to elongate much more than the cladding during rolling. However, once the proper starting thicknesses of the various components were determined these plates were fabricated without trouble.

The X 8001 and X 8002 aluminum alloys contain varying amounts of iron and nickel. These are of interest to the fuel element development program because of their corrosion resistance to high temperature deionized water. Generally, the fabrication of plates of either of these compositions can be accomplished by conventional procedures; however, cladding as thin as 0.006 in. presents some difficulties. The problem is to prevent the core ends from breaking through the thin cladding. A number of rolling schedules have been tried but in all cases the cladding has ruptured.

2.2 Sample Fuel Plate Irradiation and Testing (O. K. Shupe, M. Hatch, D. D. Jeffries)

Sample fuel plates from 22 different compositions have been irradiated in the MTR L-51 position. Some of these have been in the reactor for 14 cycles for an estimated burnup of the U^{235} of 70 to 80%. These plates indicate no visual radiation damage. Sample plates representing 10 compositions with fuel burnups from 5 to 70% were sent to the MTR Hot Cell for post-irradiation examination. These have been photographed, weighed, measured, and cut for metallographic examination.

2.3 Development of Techniques for Electron Microscope Observation of The Nature of Damage in Fuel Plates (J. M. Beeston, D. D. Jeffries)

The nature of damage in the fuel element plates is being investigated by electron microscopy of replicas of the surfaces of the irradiated fuel plates after metallographic preparation. Procedures for preparation of the replicas are reported in the literature; however, only a small percentage of the total replica is recovered on the microscope screens. One step in a procedure using cellulose acetate for replication involves the dissolution of the cellulose acetate. It has been found that a reflux technique using acetone as solvent gives good recovery if the 1/8 in. squares of the replica are placed on a microscope screen which is then placed on a refluxing screen. The refluxing screen is positioned vertically so that as the cooled reflux dissolves the cellulose acetate, the solution drains away from the replica. The replica tends to remain intact on the microscope screen.

A report [8] has been issued summarizing the progress in the Fuel Element Development Program.

3. EGCR FUEL ELEMENT DEVELOPMENT

W. C. Francis, J. R. McGeachin, E. H. Porter, M. W. Ellingford

The ETR portion of the oxide fuel development program for the Experimental Gas Cooled Reactor is now operating at full capacity with 14 capsules. Six of these capsules were inserted in the ETR in June 1959, four during December 1959, and the remaining four during May 1960. The total burnup for the capsules as of the end of this quarter ranges from 500 to 2500 Mwd/MT, which compares with a burnup objective of 3000 to 13,000 Mwd/MT. Of the capsules presently in the reactor, five are scheduled for 1600°F operation. All of the capsules to be irradiated at 1600°F and three of those to be irradiated at 1300°F have a 0.012 in. thermal barrier gas annulus. The remaining six capsules have a 0.005 in. thermal barrier gas annulus. Three types of UO_2 pellet geometries are also involved: solid, cored, and cored with BeO bushing. The fuel lengths range from 5 to 6 in.

In addition to the four capsules inserted during the quarter three capsules were moved to a higher flux region. Because of flux uncertainties in the ETR, only one of the capsules to be irradiated at 1600°F has been operated at maximum design temperature. It is expected that starting with Cycle 30 (July 1960) a flux increase will enable all capsules to be operated at their design temperature. The burnup rates will, however, for most cases be less than design. However, the design value of 35,000 Btu/hr-ft^2 of sample is actually a maximum value since only small increases above this value (e.g. 15%) can cause melting of some of the fuel cores. Reactor positions for testing were therefore selected conservatively.

4. METAL-WATER REACTION PROGRAM

W. F. Zelezny, D. E. Williams

Interest in metal-water reactions has been stimulated by considerations of reactor safety. In the event of an extreme power excursion or a loss-of-coolant accident in a water-cooled reactor, molten metal could be brought in contact with water or steam with the possibility of an explosive reaction. An experimental program has been carried out with the objective of measuring the reaction rate between water vapor and molten aluminum or aluminum-uranium alloys to determine whether an explosive hazard exists from this source. An automatically-recording thermobalance technique has been used in making these measurements.

The procedure followed is to bring the metal sample (contained in a vitrified alumina crucible) to temperature in the furnace portion of the thermobalance with a flowing purified argon atmosphere present. When the sample reaches the desired temperature, a flow of water vapor in place of the argon is introduced and weight recordings are made periodically as the argon is replaced by water vapor. Weight gains observed in this manner represent oxygen pickup by the molten metal. In all cases it is found that the weight gain vs time plots thus obtained

indicate that the oxidation follows a linear rate law. To accurately obtain the slope of this line (and hence the reaction rate) a least squares fit of this data was made to a straight line.

Runs were made at various temperatures using an aluminum - 23.4 wt% uranium alloy to approximate reactor fuel plate composition. For comparison, a similar series of runs was made using 99.99% pure aluminum. The reaction rates (in terms of gram weight gain per cm^2 per sec) thus obtained are shown graphically in Fig. 20 and 21, respectively. The confidence limits in these graphs are based on a 95% confidence level. It will be observed that each curve shows a maximum reaction rate in the neighborhood of 1800°F, and that most of the difficulty in obtaining reproducible results also occurred in this temperature range. The decline in reaction rates above 1800°F is surprising and has not yet been explained conclusively. Possibly the oxide coating becomes more coherent and protective above this temperature.

Blank runs were made with Al-U samples in a flowing argon atmosphere at 2000°F to determine whether any loss of weight due to volatilization of the aluminum was taking place. No weight change was observed; hence it was concluded that the decline in reaction rates above 1800°F is real and not due to volatilization of the sample.

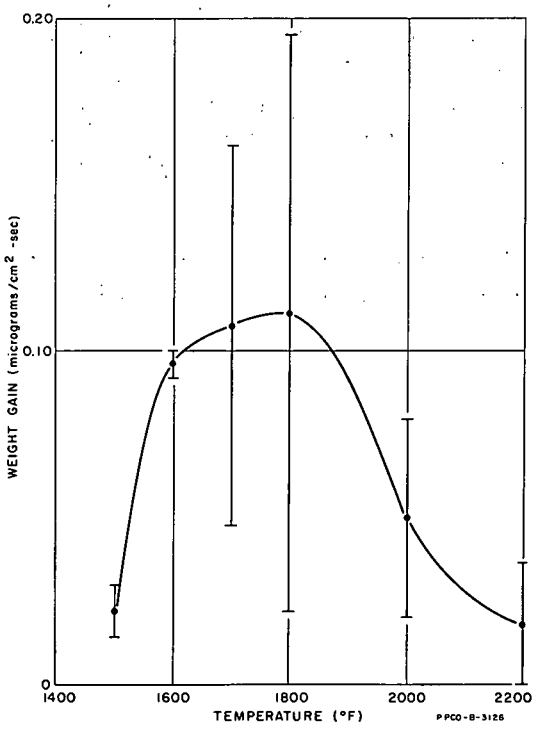

Fig. 20 Reaction rate of aluminum-23.4 wt% uranium alloy with water vapor at one atmosphere pressure as a function of temperature.

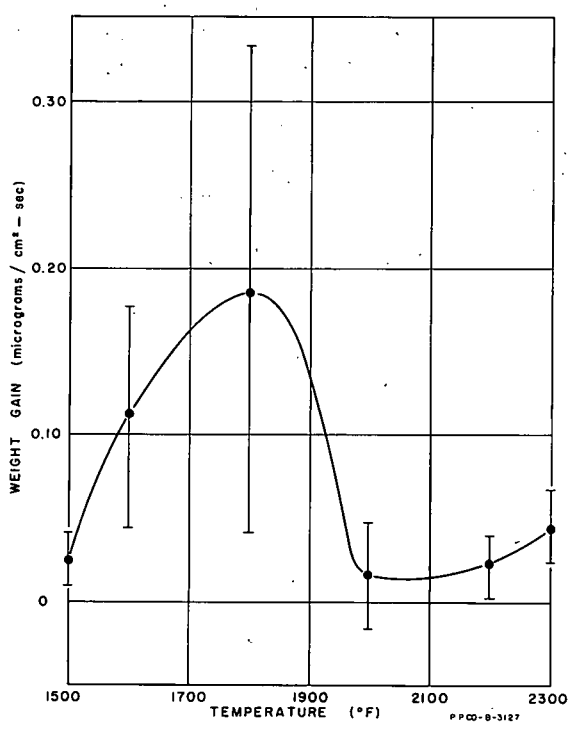

Fig. 21 Reaction rate of 99.99% purity aluminum with water vapor at one atmosphere pressure as a function of temperature.

It will be noted that these are very low reaction rates. Using the reaction rate obtained from Fig. 20 for the Al-U alloy at 1650°F, it has been calculated that the rate of heat generation corresponding to this rate of oxidation would require about 93 sec to raise a spherical molten droplet, 0.01 cm in diameter, from 1600 to 1700°F. The droplet of Al-U alloy is assumed to react with water vapor under conditions of no heat loss. These exceedingly low reaction rates, together with the decline in reaction rates at higher temperatures, could not alone cause a runaway, explosive reaction. Attention should therefore be turned to more likely metal-water reactor hazards in the transient conditions of a clean oxide-free (if possible) molten metal surface in contact with either liquid water or water vapor.

This project is being terminated at the end of FY 1960. A report summarizing the work is in progress and publication is expected during the third quarter of this year.

5. THORIUM PROGRAM

D. A. Millsap

Calculations of the heat production in irradiated RD-1 type thorium slugs have been made with consideration for maximizing the production of U^{233} + Pa^{233} before exceeding a safe heat generation rate. Using the geometry of the RD-1 type slug, as assumption that gamma heating of reactor origin in this range varies linearly with neutron flux, and concentrations of thorium irradiation-decay products calculated using an IBM program [9], the maximum allowable U^{233} content and the corresponding irradiation times were determined for a maximum heat generation rate of 500,000 Btu/hr-ft^2 for the various thermal neutron fluxes between 10^{13} and 10^{14} n/cm^{2}sec.

The contributors to the heat generation in the slug, with a surface area of 0.2025 ft^2, and the heat generation formulas determined are:

$$Q_1 = 1.786 \times 10^{-13}\ C_1\phi$$

$$Q_2 = 4.275 \times 10^{6}\ C_2$$

$$Q_3 = 1.166 \times 10^{3}\ C_3$$

$$Q_4 = 6.824 \times 10^{-10}\ C_4\phi$$

$$Q_5 = 2.248 \times 10^{-13}\phi$$

where

Q_1 = Gamma heat generation rate for the Th^{232} (n,γ) Th^{233} reaction, Btu/hr-ft^2-g of initial Th^{232}

C_1 = Ratio of Th^{232} at an irradiation time to initial Th^{232}

Q_2 = Beta heat generation rate from decay of Th^{233}, Btu/hr-ft^2-g initial Th^{232}

C_2 = Ratio of Th^{233} at an irradiation time to initial Th^{232}

Q_3 = Beta heat generation rate from decay of Pa^{233}, Btu/hr-ft^2-g initial Th^{232}

C_3 = Ratio of Pa^{233} at an irradiation time to initial Th^{232}

Q_4 = U^{233} fission heat generation rate Btu/hr-ft^2-g initial Th^{232}

C_4 = Ratio of U^{233} at an irradiation time to initial Th^{232}

Q_5 = Gamma heat generation rate from reactor origin, Btu/hr-ft^2-g initial Th^{232}

ϕ = Unperturbed thermal neutron flux, n/cm^2-sec

In general, the maximum concentrations of Th^{233} and Pa^{233} are reached before the total heat generation from the contributions above exceeds the value 500,000 Btr/hr-ft^2. An approximation can be made where the maximum values of C_1, C_2, and C_3 are used and thus determine an expression for the maximum allowable U^{233} concentration as a function of ϕ and P, the perturbation factor. This concentration is

$$C_4 = \frac{4.427 \times 10^{11}}{P\phi} - 7.254 \times 10^4$$

Where the initial thorium content is assumed to be the 1655 g typical of the RD-1 slug, this reduces the above equation to allowable U^{233} content in grams, G, before exceeding a total heat generation rate of 500,000 Btu/hr-ft^2:

$$G = \frac{7.327 \times 10^{14}}{P\phi} - 1.201 \quad .$$

The summary of the information obtained from these calculations for assumed values of thermal neutron flux is shown in Table 7. Several points of interest are apparent from these data: (1) For thermal neutron fluxes less than 3×10^{13} n/cm^2-sec, slugs can be left in the reactor indefinitely without exceeding the nominal heat generation rate limit set. The disadvantage is that a long irradiation time is required to produce a desirable U^{233} + Pa^{233} content. (2) Effective fluxes of 4 or 5×10^{13} seem to be about optimum since the desirable yield of U^{233} + Pa^{233} can be obtained before exceeding the heat generation rate limitation with favorable irradiation times. (3) Some time savings can

Table 7

SUMMARY OF IRRADIATED THORIUM SLUG CALCULATIONS

Perturbed Flux 10^{13} n/cm^{2}sec	Max Allowable U^{233} Conc, % Initial Th	Max U^{233} Content, g	Max Number 16, 5-day cycles before 500,000 Btu/ft^2-hr is exceeded	Actual Heating Btu/ft^2-hr	Actual U^{233} Content at this time, g	Pa^{233} Content at this time, g
1	4.354	72.06	--	$\ll$500,000	$<$20.0*	--
2	2.141	35.43	--	$\ll$500,000	$<$20.0*	--
3	1.403	23.22	--	$<$500,000	$<$20.0*	--
4	1.034	17.11	53	498,000	17.07	1.37
5	0.8129	13.45	26	492,000	13.23	1.73
6	0.6653	11.01	16	479,000	10.51	2.09
7	0.5599	9.29	12	496,000	9.20	2.44
8	0.4809	7.96	9	487,000	7.73	2.77
9	0.4194	6.94	7	472,000	6.48	3.07
10	0.3702	6.13	6	477,000	5.80	3.27

* It has been shown that the concentration of U^{233} can never exceed about 1.2% [10].

be obtained by irradiating the slugs in higher fluxes until the maximum heat generation rate is reached and then charging the slugs to lower fluxes until a desirable yield of U^{233} + Pa^{233} is reached.

6. NEUTRON FLUX MEASUREMENT TECHNIQUES

Co^{58} Thermal Neutron Cross Section (C. H. Hogg, L. D. Weber)

The fast neutron fluxes [10] in the MTR and ETR are now being measured by irradiating nickel and calculating the fast flux from the production of Co^{58} in the threshold reaction $Ni^{58}(n,p)\ Co^{58}$. Although a discrepancy between fast fluxes measured with nickel over various irradiation times had been suspected, it was not verified until the results from a complete ETR flux mapping program had been obtained. The discrepancy appeared conclusively between measurements made with Ni irradiated for short times in the ETR during Cycle 27 and Ni irradiated for a complete cycle. The difference was alarmingly large, i.e., up to 100%.

Obviously, then, nickel cannot be used to accurately measure the integrated fast flux in the MTR or ETR without discovering the cause of the difference and making a correction. In the belief that Co^{58} might have a large thermal neutron cross section, a program was initiated to measure the cross section and the resonance integral in several reactor locations. Preliminary results show that the total absorption cross section of Co^{58} is 1650 ± 150 b. This value was determined from measurements made in the L-45, A-38 and VH-2 facilities of the MTR where the cadmium ratios for thin cobalt are about 8, 11 and 9, respectively, and the thermal neutron fluxes are about 4.5×10^{14}, 2.5×10^{14} and 2.0×10^{14} n/cm^2-sec, respectively.

This cross section was calculated from the burnout of Co^{58} in a measured thermal neutron flux. The Co^{58}, made by irradiating Ni in a fast flux, was re-irradiated for burnout without separation from the Ni. The amount of additional Co^{58} formed in the sample during the burnout irradiation was determined by including an identical unirradiated piece of nickel in the capsule. Subtracting the induced Co^{58} activity in this sample from the total activity in the Co^{58} sample after irradiation gave the amount of activity remaining from the initial amount. Cobalt monitors placed near the Ni samples provided data from thermal flux calculations. The samples in each set (1 sample each of Ni, Co^{58} in Ni, and Co-Al alloy) were placed within 1/4 in. of each other during irradiation so that they would all receive the same nvt. The 1650 b value is the average from 40 sets of measurements. The resonance integral is probably less than 3000 b. A correction for the resonance neutron contribution to the Co^{58} burnup was made assuming that Co^{58} is a 1/v detector.

Future plans for work on this program include additional measurements of the Co^{58} cross section and resonance integral so that corrections may be applied to fast flux values. A search for another threshold reaction suitable for fast flux measurements that might be substituted for $Ni^{58}(n,p)\ Co^{58}$ is being made. The reaction $Ti^{46}(n,p)\ Sc^{46}$ is being investigated as one favorable case.

III. NUCLEAR PHYSICS

1. CROSS SECTIONS PROGRAM

M. S. Moore

1.1 Crystal Spectrometer Measurements of Eta for U^{233} (J. R. Smith)

The status of the measurements of the variation of eta for U^{233} in the region 0.01 to 1.0 ev is represented in Fig. 22. Included are the early BNL data [11], the Harwell data [12], and data obtained at the MTR by various techniques. The MTR direct measurements were all made on the crystal spectrometer using various crystal planes and filters for second order corrections as indicated in the legend of the diagram.

The computed points are from the measurements of fission and total cross sections made on the MTR fast chopper by Moore, Miller, and Simpson [13]. The solid line is calculated from parameters given by the multilevel fit to the chopper data [14]. The principle features of this curve are the following:

(1) The curve is flat within 1% between 0.01 and 0.1 ev. Some runs show a slight positive slope; others a slight negative slope.

(2) Both the MTR crystal spectrometer data and the computed data show a rise at 0.3 to 0.4 ev that is higher than that shown by the Harwell data. The multilevel fit does not show this rise, also it does not fit the fission and total cross section data in this region.

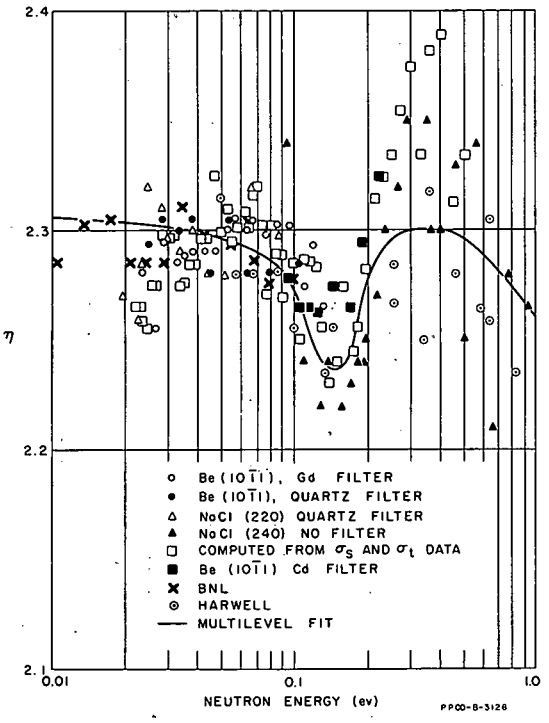

Fig. 22 Eta for U^{233} from 0.02 to 1.0 ev. This Plot represents data from BNL, Harwell, and the MTR. The MTR data were taken on the MTR Crystal Spectrometer.

Both the positive slope and the peak at 0.3 to 0.4 ev are consistent with the existence of a negative energy resonance.

1.2 Manganese Bath for Absolute Eta Measurements on U^{233} and Pu^{239} (R. G. Fluharty, J. R. Smith, S. D. Reeder, E. H. Magleby)

The Mn bath tank has been installed and aligned at the crystal spectrometer and a series of irradiations begun. These are intended to be data runs on both U^{233} and Pu^{239} as compared to the exploratory irradiations made previously. The present runs are being made at 0.057 ev with the $10\bar{1}1$ planes of Be as the monochromator, using irradiation times of about 16 hr. Both the NaI scintillation counter and the 52-tube Geiger counter system are being used to count the Mn activity. Neither has as yet demonstrated clear superiority.

1.3 Prompt Gamma-Rays from Fission of U^{233} (M. S. Moore, R. R. Spencer)

The MTR crystal spectrometer was used for studies of the prompt fission gamma spectrum of U^{233}. An attempt was made to determine the dependence of the prompt fission gamma spectrum on the spin state of the fissioning nucleus, by comparing the gamma spectra obtained by irradiating the sample with thermal neutrons and with neutrons of 1.8 ev, which correspond to the first large resonance in U^{233}.

The data obtained are being analyzed. Since a single NaI (Tl) crystal scintillation spectrometer was used in these measurements, the observed spectrum does not give the actual fission gamma spectrum. An attempt is being made to correct the observed spectrum by making measurements with a Compton anti-coincidence shield around the NaI crystal.

1.4 Coherent Inelastically Scattered Neutrons in Bragg Beams from a Be Crystal (R. R. Spencer, R. M. Brugger)

Time-of-flight analyses of the Bragg beams produced by scattering from the Be (101) and Be (103) planes were made in an attempt to detect the presence of neutrons in those beams which had undergone coherent inelastic scattering. The experimental apparatus for these measurements consists of a 3600 rpm, straight slit, slow neutron chopper mounted on the arm of the MTR crystal spectrometer, and a 1024-channel time analyzer. By mounting the chopper as close as possible to the crystal table, a flight path of 208 cm between the chopper and detector is obtained. The detector is a BF_3 proportional counter (1-in. diameter filled to a pressure of 65 cm Hg) mounted so that the uncertainty of the flight path introduced by the detector is only one inch. A magnetic pick-up provides the initiating pulse for the analyzer.

Measurements at several Bragg angles on the Be (101) beam failed to show any neutron groups which can be attributed to coherent inelastic scattering. Similar measurements taken at a Bragg angle of 23° 22' on the Be (103) planes show a resolved neutron group which is interpreted as a coherent inelastic scattering effect. The first-order Bragg

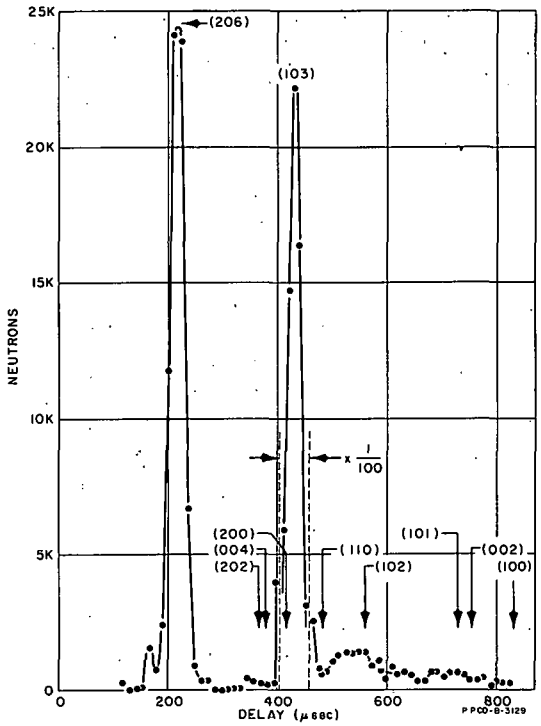

Fig. 23 Neutron counts vs flight time in μsec for the Be (103) beam at a Bragg angle of 23°22'. Arrows indicate positions at which planes in small crystallites might contribute neutrons by Bragg reflection at this angle.

neutrons at this angle have an energy of 0.125 ev. The resulting data, plotted as number of neutrons vs flight time, are shown in Fig. 23. The data have been corrected for rotor transmission and detector efficiency. A continuous background which increases slowly with decreasing flight times has been subtracted.

Neutron groups corresponding to first, second, and higher order Bragg reflections appear in Fig. 23 at flight times of 428, 214, and 162 μsec, respectively. The small neutron group between the 500 and 550 μsec flight times cannot be explained as a Bragg effect. Arrows in this figure indicate the flight times at which Bragg neutrons from planes in possible crystallites would be expected. None of these planes correspond closely to the observed group. Therefore, it is likely that this group was produced by coherent inelastic scattering. The relative intensities of the first order Bragg neutrons, second order Bragg neutrons, and this group of inelastically scattered neutrons are 100:1.3:0.2.

Neutrons scattered coherently and inelastically from a crystal must satisfy the equations:

$$\bar{k}_o - \bar{k} = 2\pi\,\bar{\tau} - \bar{q}$$

and

$$E_o - E = h\nu\,(\bar{q})$$

where $\bar{k}_o$ and $\bar{k}$ are the initial and final propagation vectors, E_o and E are the initial and final energy of the neutrons, $\bar{\tau}$ is a vector in the reciprocal lattice, and $h\nu$ and $\bar{q}$ are the energy and momentum of the waves in the crystal. For very small values of $\bar{q}$ the dispersion relation $\nu\,(\bar{q})$ is determined by ultrasonic measurements. Since the magnitude of k_o is not known for this experiment, $\nu\,(\bar{q})$ was extrapolated from the ultrasonic measurements and the above equations applied to find the values of k_o. Consistent results are obtained with initial energies between 0.058 and 0.074 ev. For these energies $\bar{\tau}$ originates from the (102) point of reciprocal space. Both longitudinal and transverse acoustical waves between the (100) and (001) directions can be

contributing. The lattice is de-excited and the neutrons gain energy. The flight time of neutrons at which the contributions from the transverse and longitudinal acoustical excitations in the (001) direction are expected, are indicated in Fig. 23.

1.5 Total Cross Section Measurements of Pa^{231} and Pu^{241} (F. B. Simpson, O. D. Simpson)

The total cross section measurements of Pa^{231} and Pu^{241} are continuing. The energy region of 0.02 to 0.20 ev has been covered for both Pu^{239} and Pu^{241}. These preliminary data are presented in Fig. 24 and 25. In order to determine the Pu^{241} cross section it is necessary to know σ_t for both Pu^{239} and Pu^{240}. The plot of preliminary data on Pu^{241} in Fig. 25 was determined by using the Oak Ridge values for the total cross section of Pu^{240} and the MTR values for Pu^{239}. Both the Pu^{239} and Pu^{241} samples are thick (transmission < 10%) for the low energy region presented here.

The high resolution total cross section measurements on Pa^{231} with the 45-m flight path are continuing, and resonance parameter determinations are in progress from the thermal region to 10 ev.

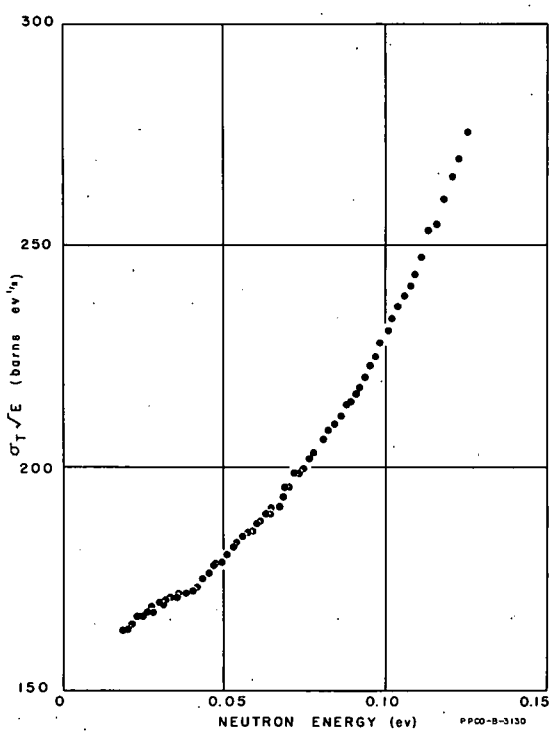

Fig. 24 Total cross section of Pu^{239} from 0.02 to 0.125 ev. These measurements were taken with the MTR fast chopper using a flight path of 16 meters and a resolution of 2 μsec/meters.

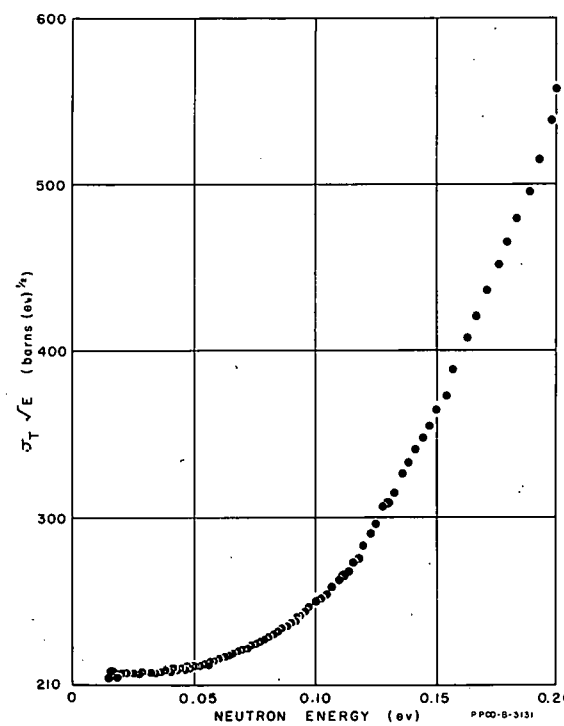

Fig. 25 Total cross section of Pu^{241} from 0.02 to 0.20 ev. These measurements were taken with the MTR fast chopper using a flight path of 16 meters and a resolution of 2 μsec/meters.

1.6 Fission Cross Section of Pu^{241} (T. Watanabe, R. P. Schuman)

The noble gas scintillation fission chamber has been assembled and pressure tested satisfactorily. Glass (multi-lead) headers presently in use will be replaced by headers having longer leads to facilitate the installation of photomultiplier tubes.

Counter characteristics are presently being measured by counting fissions produced by monochromatic low energy neutrons from the MTR crystal spectrometer test bench and from U^{235} electroplated on Ni foil (0.38 mg/cm^2). Only one of the eight subchambers is being used for this testing purpose. In addition, a fast discriminator system is also being evaluated along with these measurements.

The problem of electroplating a uniform layer of fissile material onto nickel foil over an area of 3 x 1.75 in. is being investigated. U^{235} and U^{238} foils having dimensions of 3 x 1.75 in. have been prepared by electroplating. The boundary between fissile material and backing material is well defined; however, non-uniformity of the layer of fissile material is quite evident. A technique of electroplating a more uniform layer is now undergoing study.

1.7 Fast Chopper Improvements (F. B. Simpson, O. D. Simpson)

The heavy-sample changer mounted on the drift tube has been completed and checked out for automatic operation. With this installation, it is possible to take cross section data on an extremely heavy or bulky sample by cycling it in and out of the neutron beam. It is also used to block the neutron beam automatically with a steel and B_4C slug, thus enabling a room background to be measured during each run.

2. NUCLEAR CHEMISTRY
W. H. Burgus

2.1 Beryllium Gases Experiment (R. L. Tromp)

In addition to the sample of Be mentioned in the previous quarterly report [15] two additional Be samples, taken from the highly-irradiated tensile strength coupon, were melted, their neutron-induced gases collected, and total gas volumes measured. Mass analyses have been obtained for all three gas samples and the calculated gas contents compared with the measured values. These comparisons are shown in Table 8. The measured yields from Sample 2 are somewhat open to question because of the introduction of air into the sample prior to mass analysis.

The data of Table 8 show that the total gas yields of the three samples are in fair agreement but that all three are at least 20% higher than were calculated. The latter disagreement is in part due to fairly large uncertainties in the measured fluxes and calculated fast and thermal nvt values, and in part due to uncertainties in the cross

Table 8

COMPARISON OF CALCULATED AND MEASURED GAS CONTENTS
OF NEUTRON-IRRADIATED BERYLLIUM
FROM TENSILE STRENGTH COUPON

	Calculated Yields		Measured Yield					
			Sample 1		Sample 2		Sample 3	
	cc/cc Be	v/o	cc/cc Be	v/o	cc/cc Be	v/o	cc/cc Be	v/o
He^4	6.52	93.0	7.80	89.4	8.71	91.1	7.59	88.0
He^3	0.12	1.7	0.20	2.3	0.22	2.3	0.22	2.5
$(H^3)_2$	0.32	4.6	0.43	4.9	0.26	2.7	0.42	4.9
$(H^1)_2$	0.05	0.7	0.29	3.4	0.37	3.9	0.39	4.6
TOTAL	7.01		8.72		9.56		8.62	

sections used in the calculations. Of the individual isotopic components, $(H^1)_2$ differs most strikingly from its calculated value. The measured $(H^1)_2$ content is higher by a factor of > 5 than was calculated. The most likely explanation of this is that the measured $(H^1)_2$ consists of a small amount of induced $(H^1)_2$ plus a large amount of $(H^1)_2$ impurity. The source of the $(H^1)_2$ impurity is really not known. Part of it could have been present in the un-irradiated Be but it is thought more likely that the $(H^1)_2$ had arisen from another source - perhaps from absorbed water not thoroughly evaporated by drying before the Be was melted. In this case, the hydrogen would have escaped as a gas while the oxygen would have remained with the molten beryllium (acting as a "getter"). It should be noted that although $(H^1)_2$ is apparently anomalously high it still contributes only slightly ($< 5\%$) to the total gas volume and results in small error.

The 60 samples of high purity vacuum-cast Be are continuing irradiation in the ETR. Meanwhile specifications have been drawn up and bids advertised for a cutting device for use in the MTR Hot Cell which will permit cutting samples from MTR reflector pieces. Certain pieces of the MTR reflector can now provide samples of the highest nvt-irradiated Be available. When available, these samples will be put to immediate use in swelling and gas content measurement experiments.

2.2 Half-Life of Cs^{134m} and Cross Section for Its Formation by Neutron Activation (B. Keisch)

Four more half-life determinations of Cs^{134m} were made by each of the two methods previously described in detail [16]. Briefly these consist of irradiating Cs, quickly purifying by $Fe(OH)_3$, scavenging, and precipitation of $CsI \cdot BiI_3$, dissolution of the latter compound in NaOH solution, removal of the resulting $Bi(OH)_3$ precipitate, and evaporation of a small aliquot of the Cs-containing supernate for β counting

on an end window proportional counter. For γ counting decay of the 127 kev γ peak is followed on a scintillation γ crystal spectrometer. The data of all 10 determinations have now been analyzed with the aid of the IBM-650 computer by a weighted least squares analysis method. The results, which now provide a very accurate value for the half-life, are given in Table 9.

Table 9

HALF-LIFE OF Cs^{134m}

Experiment No.	Method	Half-life, hr
1	γ-counting	2.89
2	γ-counting	2.89
3	γ-counting	2.90
4	γ-counting	2.91
5	γ-counting	2.90
	Average for γ $T_{1/2}$	2.90 ± 0.01
6	β-counting	2.91
7	β-counting	2.91
8	β-counting	2.90
9	β-counting	2.92
10	β-counting	2.93
	Average for β $T_{1/2}$	2.91 ± 0.02

Two additional determinations of the total neutron activation cross section for formation of Cs^{134m} were made as previously described [16], and two determinations were made of the effective cross section due to epi-Cd neutrons in order to correct all previously obtained values to thermal. The results are given in Table 10 and all have been corrected for K/L/M ratios (which had not previously been applied).

2.3 Yield Ratios of Isomeric Pairs by Neutron Activation (B. Keisch)

Additional measurements are being made of isomeric pair yield ratios. Such information can lead to a better understanding of nuclear reaction mechanisms in terms of shell structure theory.

Monoenergetic neutrons of 1.1 ev energy provided by the MTR crystal spectrometer were used to irradiate a 2-mil rhodium foil in order

Table 10

NEUTRON ACTIVATION CROSS SECTION FOR FORMATION OF Cs^{134m}

Experiment	Total or epi-cadmium	Cross Section, b
1	total	3.10
2	total	3.52
3	total	3.32
4	total	3.36
5	epi-cadmium	0.48 ± .05
6	epi-cadmium	0.48 ± .05

Average for total activation cross section = 3.45 ± 0.2 b

Average for cross section due to epi-cadmium neutrons = 0.48 ± 0.05 b

Thermal activation cross section (for Maxwellian spectrum) = 3.0 ± 0.2 b

to determine the yield ratio Rh^{103}/Rh^{103} with neutrons of energy corresponding to the first resonance (1.26 ev) in rhodium. The yield ratio obtained (0.081 ± 0.001) was the same as that obtained with epi-Cd neutrons (0.080 ± 0.001) but was slightly different than that obtained with thermal neutrons (0.075 ± 0.002). Since the contribution to the thermal neutron cross section by the first resonance is over 90% (as calculated from the single level Breit-Wigner formula), the small difference in yield ratio between thermal and the first resonance indicates that there must be a large difference in yield ratio between the first resonance and the negative energy resonance which is assumed to account for the small remainder of the thermal cross section. This suggests that the spin state of the compound nucleus formed by combination of the target (Rh^{103}, I = 1/2) and a neutron is different for these two resonances. The indication that at the first resonance the yield ratio increases over the thermal value also suggests that the spin of the compound nucleus at the first resonance is probably J=1 (I + 1/2), and that at the negative resonance is probably J=0 (I - 1/2), since the spin of the isomer is 5 while that of the ground state is 1. (Presumably a compound nucleus of spin 1 would favor the ground state less than that of a compound nucleus of spin 0 because of the smaller spin difference between the compound nucleus and excited state.) The assignment of J = I + 1/2 for the first resonance agrees with that of Sailor [17] which is based on a neutron resonance scattering method.

Previously determined results for the yield ratio (Y) of the isomers Ir^{192m} and Ir^{192} for thermal and epi-Cd neutrons show a large effect - Y_{epi-Cd}/Y_{th} = 0.68 ± 0.01. Because Ir^{191} has two large resonances (0.65 ev and 5.4 ev) in the epi-Cd region, both of which made

significant contributions (the higher one contributes 10% or more to the total effect in this region), a determination of yield ratio was made using both 20-mil Cd and 12-mil silver covers, simultaneously. (Silver has a large resonance at 5.2 ev.) The result, $Y_{(Cd + Ag)}/Y_{Cd}$ = 0.99 ± 0.01, indicates that the compound nucleus spin states for these resonances are the same, and that this spin is different from that for the negative energy resonance.

2.4 Neutron Flux Monitors (R. P. Schuman, J. R. Berreth)

Further work has been done on the comparison of flux monitors in VG-7. Two sets of irradiations were made. In each set the monitors consisted of Au as 0.503 wt% Au in Al alloy, Mn as Mn sponge, and Na in the form of Na_2CO_3. For each set, two irradiations were made, one unshielded and one in an 0.8-mm-thick Cd shield. All irradiations were made for the same length of time with the MTR running at constant power. The activation of the monitors was determined by absolute gamma counting. The properties assumed for the flux monitors are listed in Table 11.

Table 11

PROPERTIES ASSUMED FOR FLUX MONITORS

		Gamma Rays Counted			
Element	Activation Product	Energy, kev	Abundance of Unconverted Gamma rays,%	Thermal Activation Cross Section,b	Resonance Integral,b
Mn	2.576 hr Mn^{56}	845	98	13.3	
Au	2.698 hr	412	96.36	98.8	1558
Na	15 hr	2,750	100		

After correcting for the resonance activation, the thermal neutron flux was determined from the Au and Mn, the two monitors agreeing quite well. The resonance activation per ln E interval was determined from Au, assuming a resonance integral of 1558 b. Table 12 summarizes the thermal and resonance flux obtained for the various monitors. The resonance integral for the Mn and Na were obtained relative to the Au. Table 13 lists the thermal activation cross sections and the resonance integrals for the various monitors. The thermal activation cross section (0.583 b) and the resonance integral (0.331 b) for Na may be compared with the values of 0.536 b and 0.24 b listed by Hughes and Schwartz [18] and by Macklin and Pomerance [19], respectively.

It should be noted that the values of the thermal and resonance fluxes in the VG-7 facility, given in Table 12, should not necessarily

agree between Runs No. 1 and No. 2. This is because the whole neutron field of the MTR rises vertically as the burnout proceeds during the fuel cycle, so that the position of VG-7, relative to the "active" part of the reactor, in effect undergoes change.

Table 12

THERMAL AND RESONANCE FLUX IN VG-7

Monitor	Run No. 1 Thermal Flux, n/cm^2-sec	Run No. 1 Resonance Flux, n/cm^2-sec	Run No. 2 Thermal Flux, n/cm^2-sec	Run No. 2 Resonance Flux, n/cm^2-sec
Au	1.01×10^{13}	1.76×10^{11}	9.70×10^{12}	1.83×10^{11}
Mn	1.05×10^{13}		1.00×10^{13}	

Table 13

THERMAL ACTIVATION CROSS SECTIONS
AND RESONANCE ACTIVATION INTEGRALS FOR Au, Mn, and Na

Nuclide	Thermal Activation Cross Section, b	Resonance Integral, b	Cadmium Ratio in VG-7 Run No. 1	Cadmium Ratio in VG-7 Run No. 2
Au^{197}	standard	standard	4.63	4.36
Mn^{55}	standard	11.2	70.6	68.2
Na^{23}	0.583	0.33	102.5	99.7

2.5 Alpha Experiment (C. H. Hogg, J. R. Berreth, R. P. Schuman, R. G. Fluharty)

The irradiations of samples of pure U^{235}, U^{235} - U^{238} mixture, U^{233} - U^{238} mixture, Au-Al alloy, Co-Al alloy, Zn, and Sb flux monitor have been completed, having received an estimated nvt of 1.2×10^{21} n/cm^2. The samples are now cooling, to allow the 13-d Cs^{136} to decay away and to permit the samples to become cool enough to handle. After a total of about 3 months decay, the capsule will be opened and the ratio of Cs^{137} activity to total fissions will be determined by cesium radiochemical separations plus gamma counting, along with mass spectrometric determination of the number of fissions taking place. The experiment will also be used to compare the U^{233} and U^{235} fission and capture cross sections in the MTR L-55 position pile flux.

2.6 Decay of 5.3-d Pm^{148} and 42-d Pm^{148} (J. R. Berreth, R. P. Schuman, R. L. Heath, C. W. Reich, E. A. Yates)

Additional beta and gamma abundance data have been obtained for both Pm^{148} isomers. The abundances of the 5.3-d Pm^{148} beta- and gamma-rays are summarized in Table 14.

Table 14

ABUNDANCES OF BETA AND GAMMA-RAYS IN 5.3-d Pm^{148}

Radiation	Abundance,%
2.6 Mev β^-	45
2.1 Mev β^-	14
1.1 Mev β^-	41
1.46 Mev γ	24
0.91 Mev γ	17
0.55 Mev γ	31
2.26 Mev γ	0.05

The gamma abundances were determined on ion-exchange purified Pm samples by scintillation spectrometry and were corrected for the 42-d Pm^{148} contributions. The total beta disintegration rate was determined by end window beta counting and corrected for the contributions of 53-hr Pm^{147}, 42-d Pm^{148}, and 2.66-hr Pm^{147} obtained by gamma counting and beta decay curve analysis. Analysis of aluminum absorption curves showed high energy beta-rays (~2.6 Mev + 2.1 Mev) and a lower energy beta-ray (~1.1 Mev) in approximately the amount expected from the gamma abundances.

The gamma-ray abundances of the 42-d Pm^{148} were determined with the purified Pm samples after all the 5.3-d Pm^{148} had decayed. The abundances are summarized in Table 15. Because of the small ratio of 42-d Pm^{148} to 2.66-hr Pm^{147} activity in the sample, only very approximate beta abundance data could be obtained from the end window beta counts; however, analysis of beta decay curves did show that the 550 and 620 kev gamma-rays are approximately 100% abundant. After all the original 5.3-d Pm^{148} had decayed, aluminum absorption curves showed a small amount of high energy beta (~ 2.6 Mev) decaying with a ~ 42-d half-life. The samples also showed a low abundance 1460 kev gamma-ray. Since the spin difference between the two isomers must be quite large in order for both isomers to exist with fairly long half-lives, it is very improbable that both isomers have appreciable beta decay branches leading directly to the ground state of Sm^{148}. Consequently, the high energy beta in the 42-d Pm^{148} must arise either from beta decay to a low level, high spin state in Sm^{148} (an unlikely possibility), or from the decay of 5.3-d Pm^{148} produced by an isomeric transition decay branch in 42-d Pm^{148}. Because of the presence of the 1460-kev gamma-ray in approximately the expected abundance, as well as the 2.6-Mev beta, it seems likely that the 42-d Pm^{148} decays by a 5% abundant isomeric transition branch to 5.3-d Pm^{148}. The expected gamma abundances for 42-d Pm^{148}, assuming the isomeric transition branching, are also listed in Table 15.

Analyses of the decay curves taken on the Pm samples give half-lives of 5.3 ± 0.1 days and 42 ± 2 days for the isomers, in good

agreement with the literature values [20, 21, 22]. After more decay points have been obtained, the decay data will be analyzed using the IBM-650.

Table 15

ABUNDANCES OF BETA AND GAMMA-RAYS IN 42-d Pm^{148}

Radiation	Abundance relative to average of 620 and 550-kev gamma-rays*,%	Abundance assuming 5% isomeric transition branch to 5.3-d Pm^{148},%
2.6 Mev β^-	3.3	From 5.3-d Pm^{148}
X-ray	11	
85 kev γ	1.6	1.5
105 kev γ	2.6	2.7
185 kev γ	2.5	
280 kev γ	16	15
420 kev γ	26	25
550 kev γ	101	95% (plus a little from 5.3-d Pm^{148})
620 kev γ	99	95
720 kev γ	33	32
920 kev γ	20	19% (plus a little from 5.3-d Pm^{148})
1020 kev γ	24	23
1460 kev γ	1.0	From 5.3-d Pm^{148}

* Includes radiations from 5.3-d Pm^{148} due to isomeric transition decay of 42-d Pm^{148}

2.7 Decay of Pm^{149} (J. R. Berreth, R. P. Schuman, E. A. Yates)

In order to obtain more accurately the amount of second order capture product (53-hr Pm^{149}) in the irradiated Pm^{147} samples, some pure 53-hr Pm^{149} was produced and its end-window beta counting efficiency obtained by comparing end-window beta counts with 4π beta counts. The abundance of the 285 kev γ was also determined. The 53-hr Pm^{149} was produced by irradiating pure Nd_2O_3 in the VG-7 position of the MTR, then, after allowing 15-min Nd^{151} to decay, Nd was separated from Pm by a heated Dowex 50 cation column eluted with α hydroxy-isobutyric acid. The purified Nd was then allowed to stand overnight to allow the remaining 1.8-hr Nd^{149} to decay to 53-hr Pm^{149}, then Pm and Nd were again

separated on an ion exchange column. The Pm fraction, activity wise, was nearly pure 53-hr Pm^{149}. A sample of the Pm^{149} was 4π counted, then, was mounted in the same fashion as the irradiated Pm^{147} samples, and counted on an end-window counter through various aluminum absorbers. It was also gamma counted on a γ-scintillation spectrometer. Decay of the sample shows it to be essentially pure Pm^{149}. The abundance of the 285 kev Pm^{149} gamma-ray was 3.6 ± 0.3%.

2.8 Activation Cross Sections for Pm^{147} and the Pm^{148} Isomers (J. R. Berreth, R. P. Schuman)

Additional cross section data have been obtained for the activation of 2.66-yr Pm^{147} to 42-d Pm^{148} by irradiating Pm^{147}, both unshielded and in the Cd shield, in the VG-7 position of the MTR. The thermal activation cross section is in good agreement with the value previously reported; however, the resonance integral is considerably higher. The best present values are given in Table 16. The thermal fluxes were determined by Au, Mn, and Co monitors. The resonance flux was determined with a gold monitor assuming a resonance integral of 1558 b for gold [19].

Table 16

ACTIVATION CROSS SECTIONS OF Pm^{147}

Reaction	Thermal Cross Section, b	Resonance Integral, b
Activation to 5.3-d Pm^{148}	122	1700
Activation to 42-d Pm^{148}	108	1460
Total activation	230	3160

An additional determination of the activation cross sections of the two Pm^{148} isomers has been made. The cross sections, like those reported last quarter [23], are pile cross sections based on the pile flux as determined with Co monitors. The Pm^{147} activation cross sections used are those given in Table 16, and the assumption is made that the ratio of resonance to thermal flux seen by the samples (in the L-55 position of the MTR) is 1/30. The amounts of 2.66-yr Pm^{147}, 5.3-d Pm^{148}, 42-d Pm^{148}, and 53-hr Pm^{149} were determined by scintillation counting, end window beta counting, and analyses of decay curves. The cross sections are based both on the amounts of the two isomers and on the amount of 53-hr Pm^{149}. The results of the two determinations are summarized in Table 17.

Table 17

PILE ACTIVATION CROSS SECTIONS
OF THE Pm^{148} ISOMERS TO 53-hr Pm^{149}

Isomer	First Determination, b	Second Determination, b
5.3-d Pm^{148}	~ 0	~ 1,600
42-d Pm^{148}	18,000	20,000

3. INELASTIC SCATTERING OF SLOW NEUTRONS PROGRAM

R. M. Brugger

Data for the inelastic scattering of neutrons from methane were obtained with the MTR phased rotor velocity selector, and the curves $d^2\sigma/dE\text{-}d\Omega$ and $d^2\sigma/d\lambda\text{-}d\Omega$ were reduced from these data. The data were compared with theoretical spectra and were also condensed to the "Scattering Law" presentation proposed by Egelstaff [24]. A cold neutron facility was installed at the HG-5 hole of the MTR and 90° scattering data were obtained for vanadium.

3.1 Scattering of Neutrons by Methane (P. D. Randolph)

Methane gas is being studied as part of a program of inelastic scattering of slow neutrons from hydrogenous materials. Cross sections, differential in energy and angle, are obtained. These can be compared with theories based on particular molecular models, converted to the "Scattering Law" presentation or used directly to calculate neutron moderating processes. Further, such cross sections can be used to obtain the scattering kernels or the transport cross sections for the material, two integral values that are more familiar than the "Scattering Law" presentation to reactor engineers.

Methane was chosen as a beginning in this program for two reasons: First, since it is in the gaseous state, the dynamics of the system should be reasonably amenable to theoretical calculation. Secondly, it is one of the simplest hydrogen-containing organic molecules. Previous slow neutron studies on methane include total cross section measurements [25] and measurements of angular distributions [26] of scattered neutrons.

In the present measurements, energy distributions of scattered neutrons have been taken simultaneously at eight scattering angles from 16.5 to 83°, and with incident neutron energies of 0.023, 0.07, and 0.1 ev. For a given incident energy, a time-of-flight spectrum was obtained for a room temperature sample at each of the eight scattering angles as well as a forward beam spectrum, and recorded simultaneously in the 4096 channel time-of-flight analyzer. Fig. 26 shows a spectrum of raw

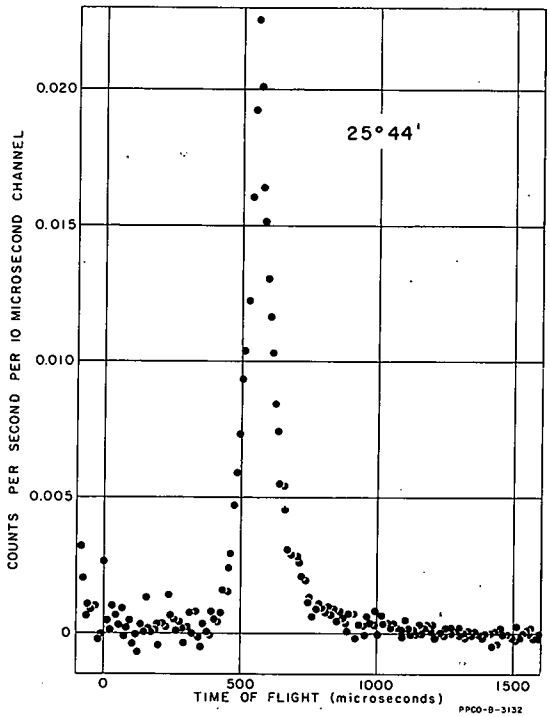

Fig. 26 Time-of-flight spectrum of 0.07 ev neutrons scattered at an angle of 26° from methane at room temperature.

data, corrected for background, at a neutron energy of 0.07 ev and at a scattering angle of 26°. Background corrections to the data are made by running an evacuated sample can in the beam. Recent measurements show that this provides a better correction than the previously used method of subtracting a run obtained with Cd in the beam. The new method corrects for fast background, air scattering in the forward beam, and to a large extent for the Bragg scattering caused by the polycrystalline nature of the aluminum sample can. The aluminum sample cans are 2 1/8 in. in diameter, have a wall thickness of 0.032 in., and are filled to pressures from 50 to 110 psi. The pressure is adjusted to make the methane approximately a 10% scatterer. The subtraction of empty holder data from the sample data does not always completely subtract the Bragg contribution, indicating that the sample cans do not have a truly random orientation of microcrystals. Cans with 0.010 in. walls are being constructed to reduce the Bragg scattering effects.

The conversion of the data to a cross section is based on calcuated counter efficiencies normalized at one energy to the beam monitor, and fluxes obtained from the beam monitor set up at the sample position. Fig. 27 shows the data of Fig. 26 reduced to a cross section in barns per ev steradian and to barns per Angstrom steradian. Fig. 28, 29, and 30 show the experimental cross sections for each of the eight angles at the incident energies 0.025, 0.07, and 0.10 ev. In these figures, the beam monitor spectrum gives the energy resolution. These data are not corrected for an angular resolution. The solid curves shown on the spectra are discussed in Section 3.3.

3.2 The "Scattering Law" Presentation (C. A. Coombes, P. D. Randolph)

The "Scattering Law" introduced by Egelstaff [24] can also be used to present the methane data. The scattering law $S(\alpha,\beta)$ is defined by

$$\frac{d^2\sigma}{d\Omega dE} = \frac{\sigma_b}{4\pi} \frac{k'}{k} \frac{e^{-\beta/2}}{k_b T} S(\alpha,\beta), \qquad (1)$$

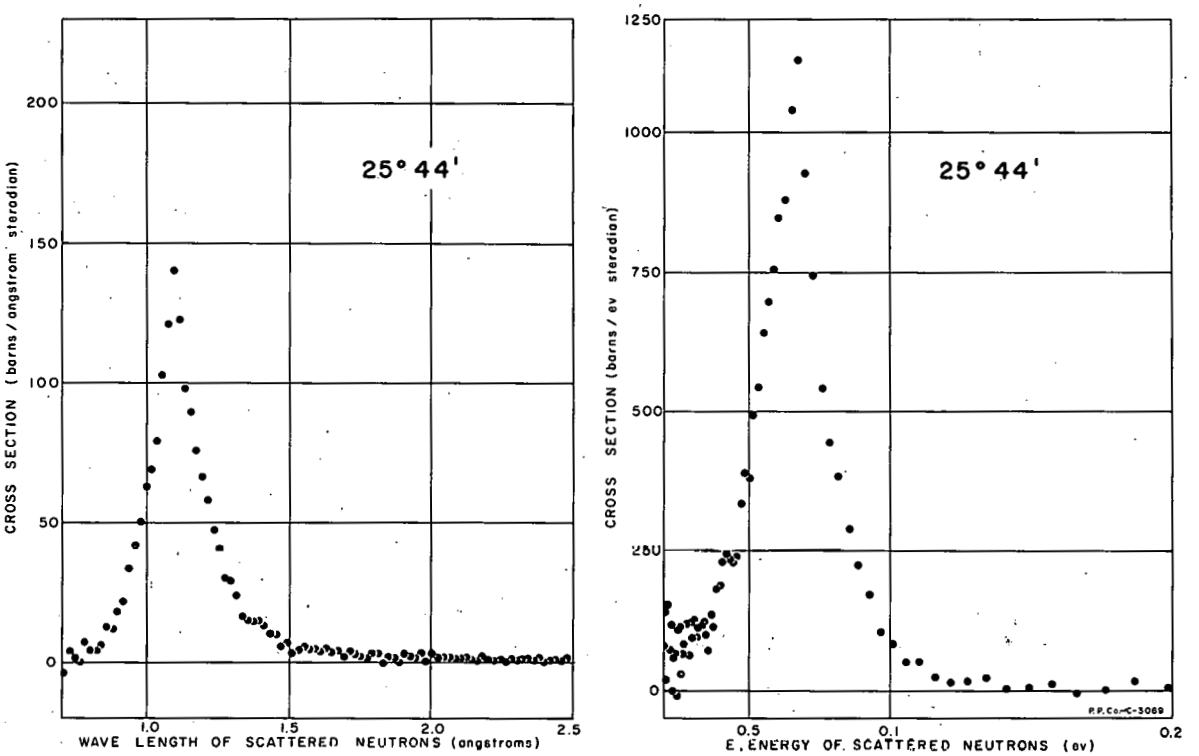

Fig. 27 The data of Fig. 26 converted to: (a) a cross section in barns per angstrom steradian, and (b) barns per ev steradian.

where

$$\alpha = \frac{(\text{Momentum transfer})^2}{2Mk_bT},$$

and

$$\beta = \frac{\text{Energy transfer}}{k_bT},$$

$\frac{d^2\sigma}{d\Omega dE}$ is the differential cross section per ev steradian at the angle θ (Fig. 28, 29, and 30),

σ_b is the bound atom cross section for hydrogen (81 b),

k and k' are the incident and scattered wave numbers,

k_b is Boltzman's constant,

T is the absolute temperature of the sample (297°K),

and

M is the effective mass of the sample (3.22 neutron masses).

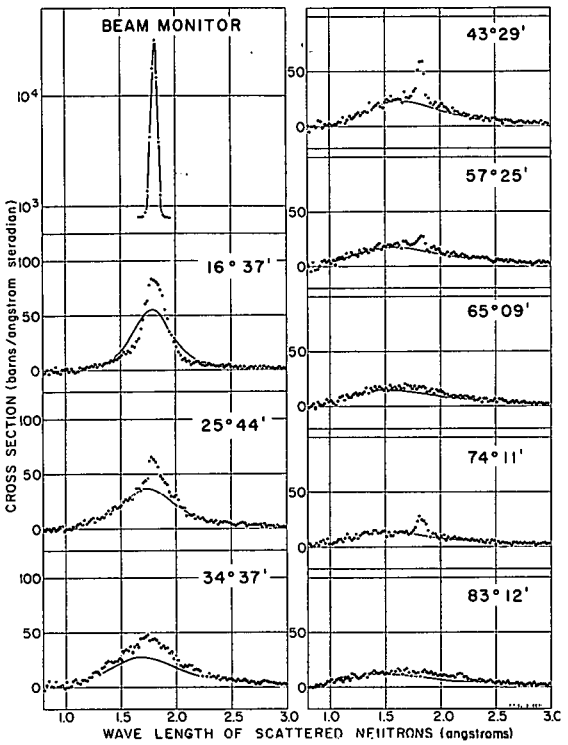

Fig. 28 Experimental cross sections for scattering of 0.025 ev neutrons from methane at room temperature as a function of wavelength of the scattered neutrons. The solid curves are theoretical fits to the data.

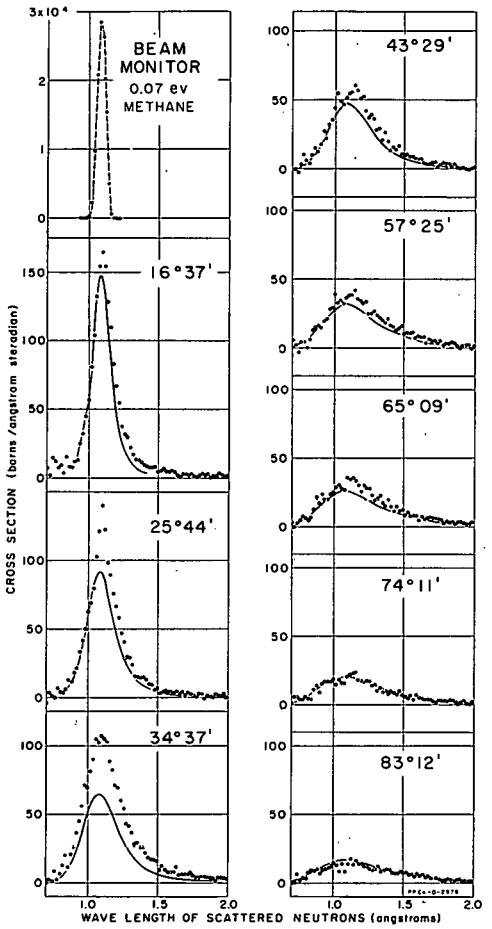

Fig. 29 Experimental cross section for scattering 0.07 ev neutrons from methane at room temperature, plotted as a function of wavelength of the scattered neutrons. The solid curves are theoretical fits to the data.

The effective mass M for methane was determined by averaging the mass tensor components suggested by Sachs and Teller [27]. Egelstaff [28] suggests using a mass equal to the most effective atom of the molecule, i.e., M = 1. This does not change the shape of the "Scattering Law" curves, but translates them. Thus, the "Scattering Law" can be obtained from the differential cross section by dividing the measured cross section by the appropriate factors given in Eq. (1). One of the main advantages of using the "Scattering Law" is that it condenses the four-dimensional data ($d^2\sigma/d\Omega dE$, k, k', θ) into three dimensions [$S(\alpha,\beta)$, α,β], i.e., the data for all incident energies, for all energies of the scattered neutrons, and for all scattering angles can be shown as a family of curves on one graph. Also, once the "Scattering Law" has been determined, it can be used to calculate the differential cross section at unmeasured energies. Egelstaff has defined the "Scattering Law" in such a manner that $S(\alpha,\beta)$ should be an even function of β; thus, for a given energy transfer, energy gains and energy losses should lie on the same curve.

Using the methane data, the "Scattering Law" has been calculated as a function of α for different energy transfers. The results are shown in Fig. 31. On each graph, the results for three different incident neutron energies are presented. Statistical uncertainties range

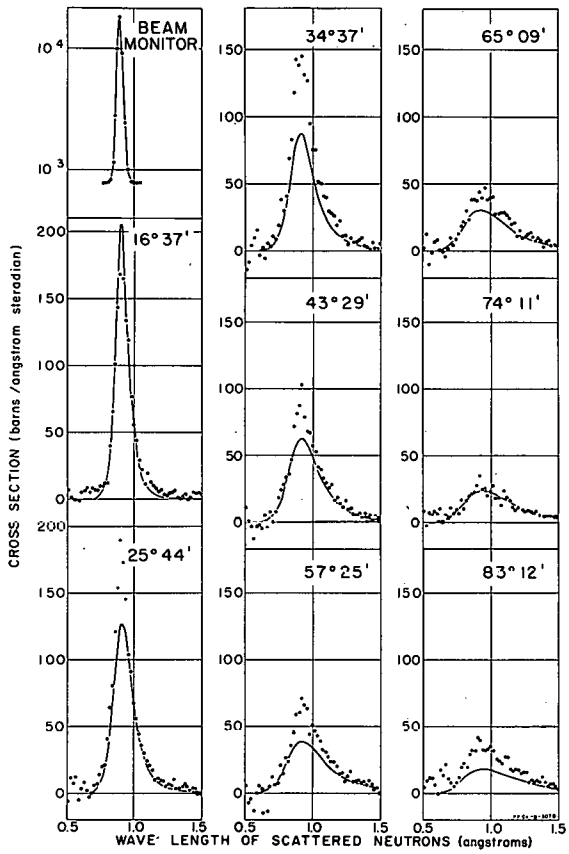

Fig. 30 Experimental cross sections for scattering 0.10 ev neutrons from methane at room temperature, plotted as a function of wavelength of the scattered neutrons. The solid curves are theoretical fits to the data.

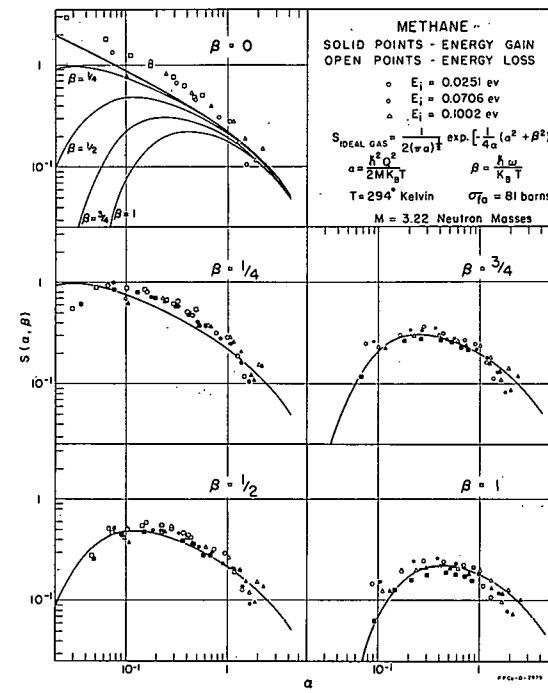

Fig. 31 The "Scattering Law" presentation of the methane data.

from 3 to 30%. At a given energy the largest uncertainties occur at the largest values of α. The smooth curves are the "Scattering Law" for a perfect gas [28]:

$$S(\alpha,\beta) = \frac{1}{\sqrt{4\pi\alpha}} \; e^{-\frac{(\alpha^2+\beta^2)}{4\alpha}}$$

By comparing the data to the perfect gas formula it is seen that the methane "Scattering Law" is very close to that of a perfect gas with an effective mass of 3.22 neutron masses. The data are not accurate enough as yet to determine whether or not rotational and vibrational states are introducing a departure from an ideal gas. The main effect of vibrational states is to lower the value of $S(\alpha,\beta)$ at the larger values of α.

One noticeable characteristic of the graphs is that the experimental data corresponding to the energy losses consistently lie slightly above the data corresponding to the energy gains. At present, the reason for this effect is not known. Appreciable air scattering of the neutrons between the sample and detectors, and errors in energy calibration could cause a splitting of the "Scattering Law" curves.

3.3 Comparison of Experimental and Theoretical Scattered Neutron Spectra for Methane (H. L. McMurry, P. D. Randolph, C. A. Coombes)

A theoretical expression has been derived for the scattering cross sections of neutrons on gases which are differential in energy and angle (see Section 4). The assumption is made that there is a continuum of rotational states present in the energy range of interest but that no vibrational states are excited.

The results of the theory as applied to the scattering of neutrons from methane are shown as the solid curves in Fig. 28, 29, and 30. The main features to be noticed are:

(1) At forward angles the experimental measurements yield higher cross sections than the theory. As the angles get larger the agreement becomes better.

(2) The widths at half maximum of the theoretical profiles are at least as wide as the experimental widths.

(3) At forward angles the experimental maxima occur at longer wavelengths than the theoretical.

The disagreement in the cross section values at forward angles could be partially attributed to an error in measuring the absolute counter efficiencies, and partially due to incomplete subtraction of the Bragg scattering contribution of the sample holder. Since the scattering law presentation of the data (Section 3.2) is a fairly smooth curve it is unlikely that the error in obtaining the counter efficiencies is very large. To reduce the effects of Bragg scattering, sample holders with 0.010 in. walls are being made to replace those with 0.032 in. walls. The theoretical profiles shown have not been broadened by the energy resolution of the apparatus. Since the theoretical widths without energy resolution broadening are already as large as the experimental widths, the theory predicts too broad a spectrum. Also, it is to be noted that, especially at forward angles, the maximum of the theoretical wavelength profile occurs at the wavelength of the incident neutrons, whereas the experimental maximum is at longer wavelengths. At large angles the discrepancy is not as pronounced. This experimental shift to longer wavelengths could be caused by any process that tends to increase the apparent number of energy loss processes, such as double or plural scattering in the target material or air scattering of the neutrons between the target and the detectors. These would result in false time-of-flight indications since the neutron flight path would be increased.

The conclusion that can be drawn at this stage is that though experimental errors could be causing discrepancies in the maximum values of the cross section and a shift of the maximum to longer wavelengths, the theory is not completely correct since at least for forward angles it predicts too broad a spectrum.

3.4 Velocity Selector Modifications

3.41 Rotating Collimator Position Change (P. D. Randolph) The installation of the permanent shielding around the scattering room and the fitted shielding around the velocity selector resulted in appreciably reduced backgrounds, the most noticeable change being in the reduction of room background. The fast background, resulting from fast neutrons in the reactor beam penetrating some or all of the rotors when they are closed, and from scattering by the rotors inside the scattering room and from the sample, was also reduced. Further background reduction can best be accomplished by reducing this fast background component.

The pair of rotating collimators spaced 0.5 m apart was shifted 0.5 m closer to the reactor and to the first chopper. This removed the second collimator from its position at the beam entrance to the scattering room, thus reducing the background effect of neutrons scattered from it when in the closed position. Also, since the rotating collimators are located closer to the first chopper, they close earlier in the cycle so that they introduce more material in the beam at the time the detectors are counting the slow neutrons scattered from the sample. This move has resulted in a reduction of the fast background by a factor of about two.

3.42 Shielded Counter Racks (P. D. Randolph) Aluminum cans filled with B_4C have been installed to reduce the number of scattering room background neutrons entering the velocity selector detectors. These cans are mounted on the counter support racks. They place a layer of B_4C 0.5-in.-thick on the top, bottom, and at the back of the counters. Also, the B_4C covers the front of the counters except for an 18-in.-high band facing the sample. Installation of the racks is planned for early August.

3.43 Differences in BF_3 Detector Characteristics (K. A. Strong) A shipment of 80 BF_3 counters (18-in. active length, 15/16-in. inside diameter, 0.006-in. center wire, and filled with enriched BF_3 to a pressure of 120 cm Hg) has been received, and an integral bias curve has been run on each counter. During tests, it was found that the gain requirements were greater for these counters than for the counters now in use on the velocity selector. This difference indicates a difference in counters that were supposedly similar, possibly in gas pressure or the size of the center wire. To obtain the needed gain, two preamplifiers were connected in series, replacing a single one. Satisfactory bias curves were obtained with this modification. Ten of these counters are presently in use with the cold neutron facility.

3.44 4096 Channel Analyzer (R. B. Kennedy) Modification of the 4096 channel analyzer is in progress to eliminate interangle feedback, i.e., the storing of information from one angle in the storage locations of another angle. This feedback is caused by random input pulses which are not of sufficient amplitude to set the angle storer flip-flops to the correct angles. This interangle feedback is being eliminated by installing trigger circuits (which give an output pulse of constant amplitude when driven with an input pulse of 6 v or more) for each

angle. The trigger circuits will not trigger with an input of less than 6 v. Since the angle storer flip-flops will be driven with constant amplitude pulses from the trigger circuits, they will be set to the correct angles, eliminating this source of the interangle feedback.

3.5 Rotor Transmission Calculations (K. A. Strong, R. M. Brugger)

To facilitate the design of rotors which are more efficient scatterers of fast background neutrons, the theoretical transmission of the velocity selector rotors is being studied by means of a recently developed IBM computer program. This program is designed to determine how many neutrons between 1 and 20 Mev are transmitted by the rotors of the velocity selector and enter the experiment as fast background.

The path lengths through each material in the rotor have been computed for a set of 15 parallel paths p through the rotor at various angles to the beam. For a given set of rotor materials m, with corresponding path lengths X_p, cross section data σ_{mE}, and a given incident flux R_E, the program will compute the transmission as a function of angle. The following are the basic calculations: For a given angle α, the number of neutrons (T_{pE}) of energy E that get through path p is

$$T_{pE} = N_o e^{-\sum_1^m \eta_m X_{pm} \sigma_{mE}},$$

where m is the material, N_o is the initial number of neutrons in the particular path incident on the rotor, η_m is the number of atoms per cm^3 of material m, and X_{pm} is the path length in material m for a particular path p.

The number of neutrons for all energies that get through path p is

$$T_p = \sum_1^E R_E T_{pE},$$

where R_E is the weighting factor for each energy interval.

The number of neutrons that get through all paths is

$$T = \sum_1^p T_p,$$

$$= \sum_1^p \sum_1^E R_E N_o e^{-\sum_1^m \eta_m X_{pm} \sigma_{mE}} .$$

Finally, this result is normalized to unit flux by

$$\underset{\sim}{T}(\alpha) = \frac{\sum_{1}^{p}\sum_{1}^{E} R_E N_o e^{-\sum_{1}^{m} \eta_m X_{pm} \sigma_{mE}}}{\sum_{1}^{p}\sum_{1}^{E} R_E} .$$

This program should facilitate design of rotors for optimum reduction of fast background when rotors of different design are made from different materials.

3.6 MTR Cold Neutron Facility (R. M. Brugger, R. E. Schmunk)

A cold neutron facility has been installed at the MTR and preliminary inelastic scattering data have been obtained. This facility will be used to make survey measurements of inelastic scattering events, with the result that the velocity selector time will be conserved for more detailed measurements. With this facility the presently proposed experiments include the measurements of: (1) the rotational states of water and methanol, (2) continuation of the dispersion curve measurements for single crystals of Be, (3) a check of the frequency distribution of vanadium, and (4) preliminary measurements of samples to be used on the velocity selector.

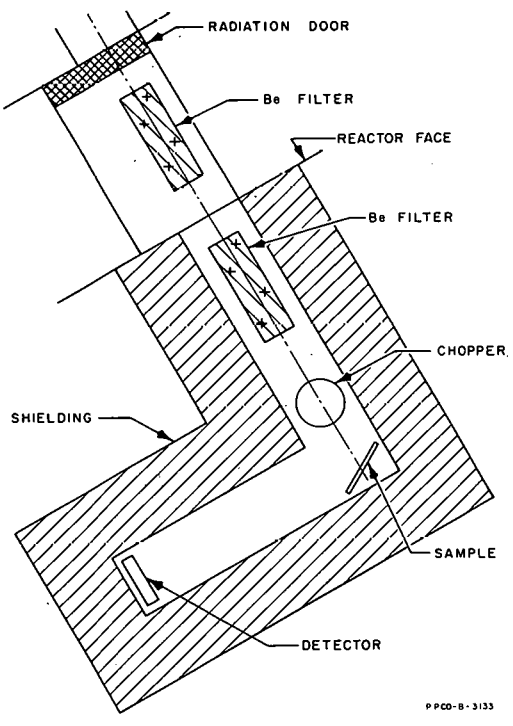

Fig. 32 The MTR Cold Neutron Facility.

The MTR cold neutron facility was assembled at the northeast corner of the MTR with the HG-5 beam hole as a source of neutrons. The 1-ft thick lead radiation door of this hole is used as a beam stopper when changes are made to the external experimental equipment (Fig. 32). Between this door, which is 32 in. inside the face of the reactor biological shielding, and the face of the reactor is placed a 16-in. long by 5-in. diameter piece of reactor grade beryllium with its associated liquid nitrogen jacket and vacuum insulation. The 1-ft thick lead door and 16 in. of beryllium are adequate, when the reactor is at 40 Mw, to suppress the beam outside the reactor to 10 mrem/hr fast neutrons, 300,000 c/sec cm^2 slow neutrons, and 40 mrem/hr gammas. The fast neutrons that penetrate the first filter are undesirable experimentally and another filter of

16 in. of liquid nitrogen cooled beryllium is placed in the beam immediately outside the reactor Thus, the total filter system of the MTR cold neutron beam facility is 32 in. of liquid nitrogen cooled beryllium which passes about 60% of the neutrons below 0.005 ev.

One of the spare choppers of the velocity selector, having curved slits with 0.032-in. spacings and a 2-in. chopping radius, is placed after the second filter. This chopper allows a 4-in. high by 1 1/3-in. wide beam to pass to the sample that is placed after the chopper in the beam 9.72 in. from the center of the chopper. A set of BF_3 detectors is placed about 1.75 m from the sample at 90° to the beam. The filters, chopper, sample, and counters are shielded with neutron shielding and a lead beam catcher is placed after the sample.

Fig. 33 shows some of the properties of the beam of cold neutrons. A 1/16-in. thick sample of vanadium metal was placed at the sample position and the counting rate, as a function of time-of-flight after the chopper opened, was recorded by means of the 100-channel time analyzer with 10-μsec channels and about 1.7 msec initial delay. The neutron counting rate rises at the Bragg cut-off in 55 μsec with the half-height at 3.96 Å. At longer flight times, the counting rate decreases more rapidly than is observed with most beryllium filtered beams because of the added length of the beryllium and because of the transmission properties of the chopper which is placed before the sample. That is to say, these effects improve the energy resolution of the initial beam by their velocity discriminating actions. For this particular case, the effect is pronounced enough to make the filter difference method, using Be and Pb filters as used by some experimenters, unnecessary. Another advantage of chopping the beam before the sample is that the curvature of the slits of the chopper can be selected to give maximum transmission for the incident neutrons and all inelastically scattered neutrons of all energies will be observable. Also the solid angle subtended by the counters is not limited by the collimation of the chopper. The disadvantage of having the chopper before the sample is the time uncertainity introduced by the different energy neutrons traveling from the chopper to the sample. In the present case, this amounts to a 25 μsec difference between 4 and 4.3 Å neutrons. The mean wavelength of beryllium filtered neutrons is 4.3 Å.

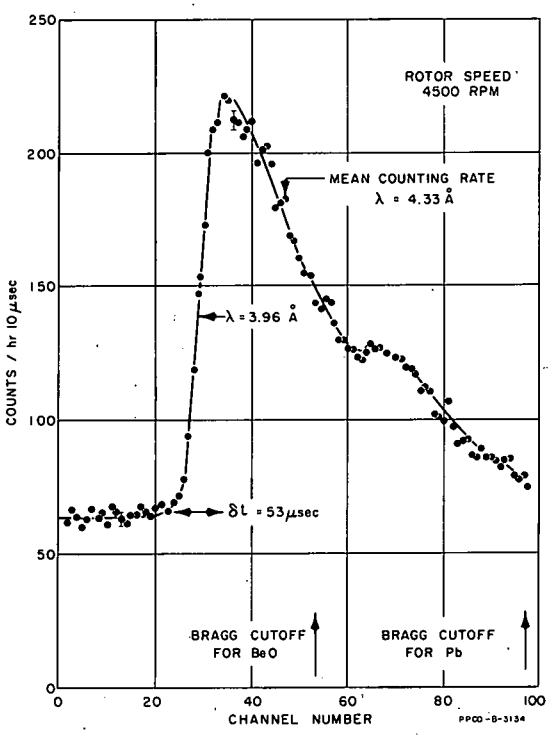

Fig. 33 Properties of Be filtered neutrons scattered by 1/16 in. vanadium sample.

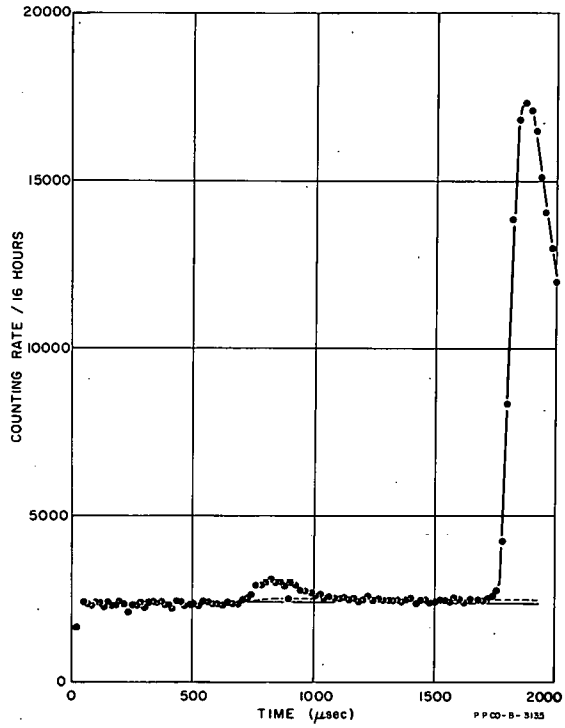

Fig. 34 Time spectra of beryllium filtered neutrons scattered by a 3/16 in. sample of vanadium. The solid line is the time independent background. The dotted curve is the effect due to air scattering. The effects between 800 and 1000 μsec is the inelastic scattering due to vanadium. [The difference between the experimental data curves and the time independent background plus air scattering curve (in the range from 800 to 1000 μsec) is the inelastic scattering due to vanadium.]

Fig. 34 shows the inelastic scattering effects observed from a 3/16-in. sample of vanadium. A small effect from air scattering in the vicinity of the sample is observed and the data must be corrected for this and the time independent background. Suppression of the time independent background will be achieved in the future by the addition of fitted shielding.

4. DECAY SCHEME STUDIES

R. L. Heath

The Decay of 15-Day Eu^{156} (J. E. Cline, R. L. Heath)

The study of the decay of Eu^{156} has been completed and the results have been prepared for publication. Recent work on this nuclide has concerned itself with attempts to determine the spins and parities of some of the previously reported [29] energy levels in Gd^{156}.

Gamma-gamma directional correlation measurements were made on the 810-1060, 810-1150, 650-1230, 89-1940, and 89-2100 kev gamma-ray cascades. Measurements were limited to these few cascades because of the complexity of the gamma-ray spectrum. The criteria were that the gamma rays could be adequately resolved in the singles spectrum and that the coincidence relationships were simple. Multipolarities had been assigned to these gamma rays by Ewan et al. [30], on the basis of internal conversion coefficient measurements.

The source material was prepared in dilute HCl solution and was contained in thin-walled lucite holders, 1/16-in. ID. Gamma-ray detectors used in the experiment were 3-in. NaI(Tl) crystals mounted on Dumont-6363 photomultiplier tubes. The source-detector distance was 10 cm. Coincidence circuitry was of the "fast-slow" type with a resolving time 2τ of ~ 0.08 μsec. Data were taken in 9-degree increments from 90 through 180°. Three determinations of the coincidence counting rate were made at each angle, each determination containing about 900 counts. The random coincidence rate was measured and was found to be $\sim 3\%$ of the gross coincidence rate.

Table 18 lists the results of the angular correlation measurements. These data could be fitted with Legendre polynomial expansions containing no polynomials of an order higher than 2. In all cases, the coefficient of the $P_4(\cos\theta)$ term is not statistically significant. The 810-1060 and 810-1150 cascades from the state at 1960 kev contained gamma rays of known multipolarity and proceed through an intermediate state of known spin to final states of known spins. The only unknown quantity, then, is the spin of the initial state. In the 650-1230 kev cascade, although the multipolarities were known, the spin of the intermediate state was not definitely established. These three measurements served, therefore, to determine uniquely the spins of the levels at 1960 and 1320 kev as 1 and 2, respectively. The parities were known from the gamma-ray multipolarities. The results of the measurements of the 89-2100 kev gamma-ray cascade failed to determine uniquely the spin of the level at 2200 kev. The difficulty lies in the fact that the measured correlation function is consistent with either a 1(1)2(2)0 or a 2(1)2(2)0 spin sequence, each requiring a different mixing parameter for the 1940 kev transition. A more precise measurement of the correlation function is necessary in order to distinguish between the two possibilities. Due to the low coincidence counting rate in this experiment, such a precise measurement could not be made at this time. The correlation function for the 89-1940 kev gamma-ray cascade may be fitted uniquely by assuming a 1(1)2(2)0 spin sequence. A level scheme for Gd^{156} incorporating the results of these measurements is shown in Fig. 35.

Table 18

EXPERIMENTAL COEFFICIENTS OF P TERMS IN γ - γ ANGULAR CORRELATION MEASUREMENTS AND SPIN SEQUENCE ASSIGNMENTS

Level Sequence Energies, kev	Coefficient of P_2 Term	Spin Sequence of Levels
1960(810)1150(1060)89	-(0.011 ± 0.010)	consistent with 1(1)2(1)2 with mixing
1960(810)1150(1150)0	-(0.145 ± 0.023)	1(1)2(2)0 with mixing in first gamma ray
1960(650)1320(1230)89	-(0.137 ± 0.015)	1(1)2(1)2 with no mixing (all E1 radiation)
2200(2100)89(89)0	+(0.128 ± 0.020)	either 1(1)2(2)0 or 2(1)2(2)0
2030(1940)89(89)0	-(0.135 ± 0.029)	1(1)2(2)0 with mixing in first gamma ray

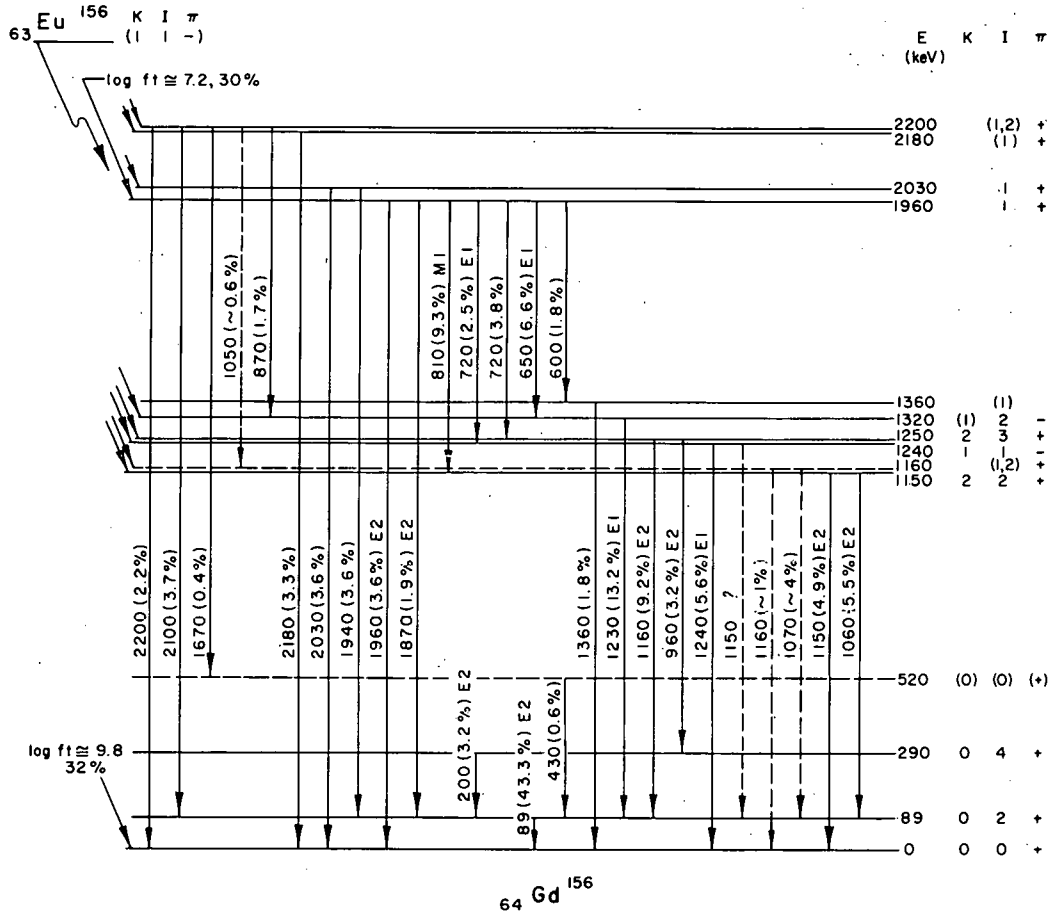

Fig. 35. A level scheme for Gd^{156} incorporating results of new decay measurements.

5. EXPERIMENTAL TECHNIQUES AND INSTRUMENTATION

MTR Crystal Spectrometer Shielding Cart Drive Study (S. R. Gossmann, R. H. Brown)

It is contemplated that the speed of the drive unit for the MTR Neutron Crystal Spectrometer arm will be increased by a factor of 10. If this is done, the speed requirements for the shielding cart drive will also be increased by a factor of 10. There is some doubt about its ability to meet this increased speed requirement while maintaining the original specifications for close tracking of the arm. To check this possibility it became necessary to perform a dynamic analysis of the system. Because of the several non-linearities in the system, an analytic expression for the time behavior of the system cannot be obtained. However, the problem is ideally suited for solution on the Electronic Differential Analyzer (EDA).

This system possesses four types of non-linearities. They are saturation in the amplifiers, velocity limiting in the motor, coulomb friction in the motor, and backlash in the gears. The various functions

representing these non-linearities were generated with special circuitry as shown in Fig. 36.

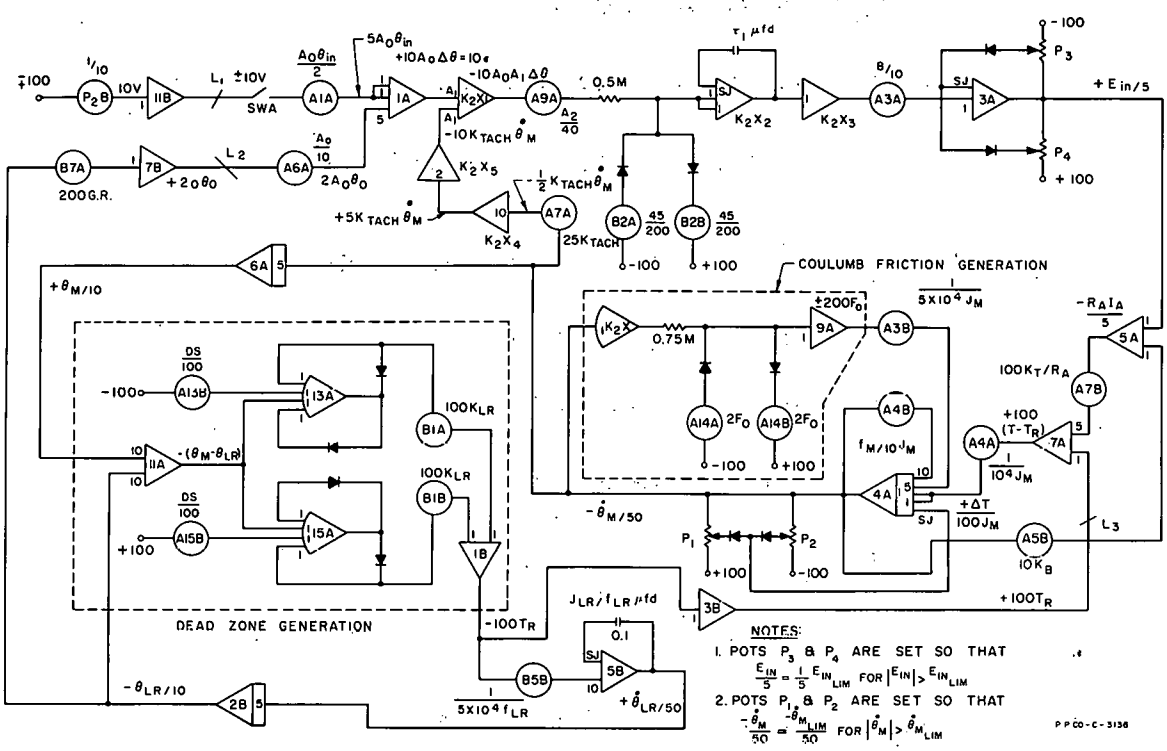

Fig. 36 Computing element interconnections to solve the differential equations for the MTR Crystal Spectrometer shielding cart drive study.

The differential equation of motion of the system and values of all the system parameters were supplied by the design engineer. The system is described mathematically by the following set of equations:

$$J_m \ddot{\theta}_m + f_m \dot{\theta}_m \pm F_o (\dot{\theta}_m) = T - T_{LR} \quad , \text{ with } \dot{\theta}_m \leq \dot{\theta}_{m_{LIM}}$$

$$T = K_T I_A \quad ,$$

$$R_A I_A = E_{in} - e_B \quad ,$$

$$e_B = K_B \dot{\theta}_m \quad ,$$

$$T_{LR} = K_{LR} F_1 (\theta_m - \theta_{LR}) \quad ,$$

$$J_{LR} \ddot{\theta}_{LR} = T_{LR} - f_{LR} \dot{\theta}_{LR} \quad , \text{ and}$$

$$\theta_o = G.R. \theta_{LR} \quad .$$

where

$\dot{\theta} = \frac{d\theta}{dt}$

θ_m = motor shaft position

J_m = moment of inertia of motor

f_m = coefficient of viscous friction

$F_o(\dot{\theta}_m)$ = coulomb friction torque (Fig. 37)

T = torque applied to motor

K_T = motor torque constant

I_A = motor armature current

R_A = motor armature resistance

e_B = back e.m.f.

K_B = back e.m.f. (coefficient)

The LR subscript refers to cart parameters reflected back through the gear box:

$F_1(\theta_m - \theta_{LR})$ = dead zone function (Fig. 38)

G.R. = gear ratio

θ_o = cart position

E_{in} = output of magnetic amplifier

The LIM subscript refers to the limit or saturation value of the quantity.

The control system equations are:

$$\epsilon = A_o(\theta_{in} - \theta_o) \quad ,$$

$$\tau_1\dot{E}_1 + E_1 = A_1\,\epsilon - K_{TACH}\,\dot{\theta}_m \quad \text{for} \left| E_1 \right| \leq E_{1_{LIM}}$$

$$E_{in} = A_2\,E_1 \quad . \qquad \text{for} \left| E_{in} \right| \leq E_{in_{LIM}}$$

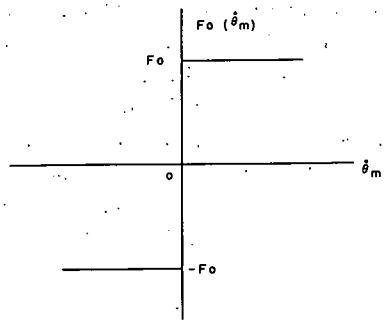

Fig. 37 The coulomb friction torque of the MTR Crystal Spectrometer cart drive motor.

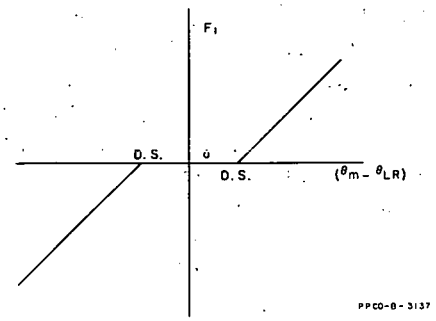

Fig. 38 The backlash in the gears of the MTR Crystal Spectrometer cart drive showing the dead zone, D. S.

where

θ_m = motor shaft position

θ_o = cart position

θ_{in} = demand signal to cart drive system

A_o = transducer gain

ϵ = error voltage

E_1 = output of operational amplifier

A_1 = gain of operational amplifier

τ_1 = time constant of operational amplifier

A_2 = gain of magnetic amplifier

E_{in} = output of magnetic amplifier

K_{TACH} = gain of tachometer

The function F_o ($\dot{\theta}_m$) , the coulomb friction torque, varies with velocity as shown in Fig. 37. The backlash in the gears can be represented as a dead zone in T_{LR} (the torque on the load reflected back through the gears) as shown in Fig. 38. The quantity ± DS is the width of the dead space. The arrangement of computing elements required to solve these equations is shown in Fig. 36.

Because of the complexity of the problem, no analytical checks were available. Some of the less certain parameters were varied until the time behavior of the voltages representing the positions and velocities of the system appeared to be right as compared to the actual time behavior of the cart drive system. At that time it was felt that a reasonably accurate representation or model of the system had been attained. It was then possible to investigate the response of the cart drive to a demand signal calling for 10 times normal speed and evaluate the effect of control system parameter changes on the system response.

The results conclusively indicate that the cart drive unit, with suitable amplifier modifications, will be capable of meeting the new requirements.

IV. THEORETICAL PHYSICS AND APPLIED MATHEMATICS

1. THEORETICAL WORK RELATED TO THE SLOW NEUTRON SCATTERING PROGRAM

H. L. McMurry

The Krieger-Nelkin approximation [32] for calculating differential cross sections with respect to energy and angle has been shown to compare favorably with a more rigorous but computationally more difficult approach, and to give good overall agreement with experimental data on CH_4. Average values of energy transfer $\epsilon(\theta,E)$ and $\epsilon(E_0)$ have been calculated for CH_4 in the range E_0 = 0.003 to 0.1 ev using results from the K. N. method.

1.1 Comparison of Procedures for Calculating Differential Cross Sections

(H. L. McMurry, G. W. Griffing, L. Gannon, W. Hestir)

Two methods for calculating differential cross sections of gases with respect to energy transfer ϵ and angle have been tried in this laboratory. Both are based on the formulation of Zemach and Glauber [31] and assume that the rotational motion can be treated classically, that the vibrations are governed by a quadratic potential function, and that effects due to rotation-vibration interaction and centrifugal stretching are negligible. In both cases $d^2\sigma/d\Omega d\epsilon$ is expressed as a sum of terms for scattering by each atom in the molecule, together with terms for coherent scattering by pairs of atoms.

One method, the Krieger-Nelkin approximation [32], assumes that the thermally averaged expectations associated with scattering by individual atoms, or pairs of atoms, can be expressed as a product of expectations for the translational, rotational, and vibrational motions, and that the average of these products over molecular orientations is equal to the product of the averages for each factor. Furthermore, certain exponential factors which depend on orientation are averaged in the exponent. For any given atom one of these factors is the Sachs-Teller mass tensor and its average over orientation in the exponent yields an effective mass which depends on the position of the atom, the moments of inertia, and the total mass of the molecule [32]. This averaging procedure leads to an expression for the incoherent part of $d^2\sigma/d\Omega d\epsilon$ which is a sum of terms for scattering by the different atoms in which each term has the form of the scattering law for a monatomic gas with mass equal to the effective mass for this atom.

The other method [33] is more rigorous in that the expectation is not approximated by a product, and the averages over molecular orientation are obtained by machine calculation.

The K. N. method is relatively easy to use and it is desirable, therefore, to see how it agrees with experiment and with the more rigorous method. For neutron energies of 0.1 and 0.07 ev, the two methods agree almost exactly over the range of comparison, which includes angles up to 83°. For 0.025 ev neutrons, the results agree at 16°. At 43 and 83°, the maxima by the more exact method are shifted slightly toward lower energy relative to that on the K. N. method. At 83° this shift is about 0.003 ev. The two methods are equally good as a basis for comparison with current data in this energy range.

1.2 Application of the Krieger-Nelkin Method to Calculation of $d\sigma/d\Omega$ and σ for CH_4 (G. W. Griffing, L. Gannon)

The overall agreement between experimental values of $d^2\sigma/d\Omega d\lambda$ for CH_4 and those calculated by the K. N. method is good, although there are significant discrepancies at forward angles. Experimental data on CH_4 for $d\sigma/d\Omega = \int (d^2\sigma/d\Omega d\lambda)\, d\lambda$ and $\sigma = \int (d\sigma/d\Omega)\, d\Omega$ are also available. Since these quantities can be readily calculated by machine, using results from the K. N. method, it is interesting to see if discrepancies of the order of those found in $d^2\sigma/d\Omega d\lambda$ persist.

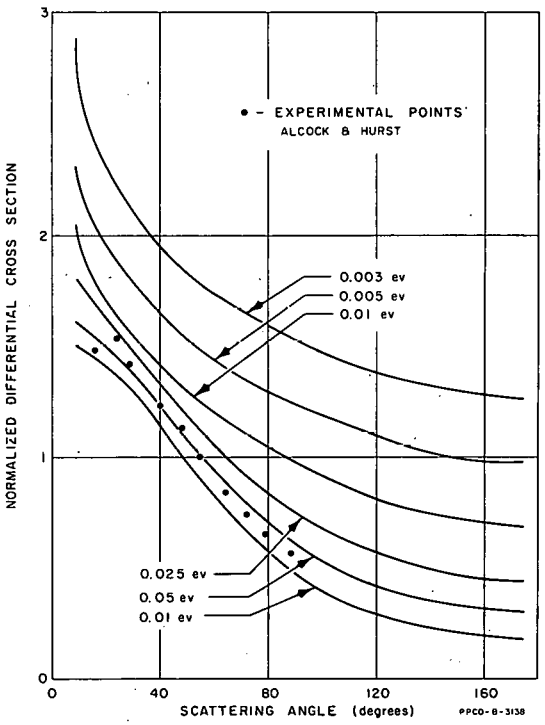

Fig. 39 Differential cross section for neutrons scattered from methane as a function of the scattering angle for various impact energies. The experimental points are for an impact energy of 0.073 ev. The differential cross section is such that

$$\int (d\sigma/d\Omega)\sin\theta d\theta$$

will give the total cross section per hydrogen atom. For absolute values of the differential cross section per hydrogen atom the number from the curve is to be multiplied by 28.5 barns.

Fig. 39 shows the calculated dependence of $d\sigma/d\Omega$ on scattering angle for several impact energies. These results were obtained by numerical integration of the $d^2\sigma/d\Omega d\lambda$ data. Also included are the experimental data of Alcock and Hurst for 0.073 ev neutrons [26]. The theoretical curve for the energy has been omitted from Fig. 39 in the interest of clarity, but it would lie approximately half-way between the curves for 0.05 and 0.1 ev impact energies. The experimental results have been normalized to the theoretical at 87.7°. It is seen that the theoretical $d\sigma/d\Omega$ is low relative to the experimental values at the forward angles. This is consistent with the fact that the calculated values of $d^2\sigma/d\Omega d\lambda$ are also low relative to the experimental values at forward angles. However, the arbitrary manner in which the experimental data have been normalized to the theoretical at 87.7° rules out making this

deduction solely on the basis of a comparison of the experimental and theoretical results plotted in Fig. 39.

The experimental values of σ obtained by Melkonian [25] are compared with the calculated σ values in Table 19. The agreement is exact to within the accuracy with which Melkonian's curve can be read.

Table 19

COMPARISON OF CALCULATED AND EXPERIMENTAL TOTAL CROSS SECTIONS PER HYDROGEN ATOM IN METHANE

E_o, ev	0.003	0.005	0.01	0.025	0.032	0.043	0.05	0.07	0.1
Theory σ, barns	91.9	75.4	59.5	47.8	45.2	42.7	41.0	37.9	34.0
Experiment σ, barns	93	75	59	46	45	43	42	36	32

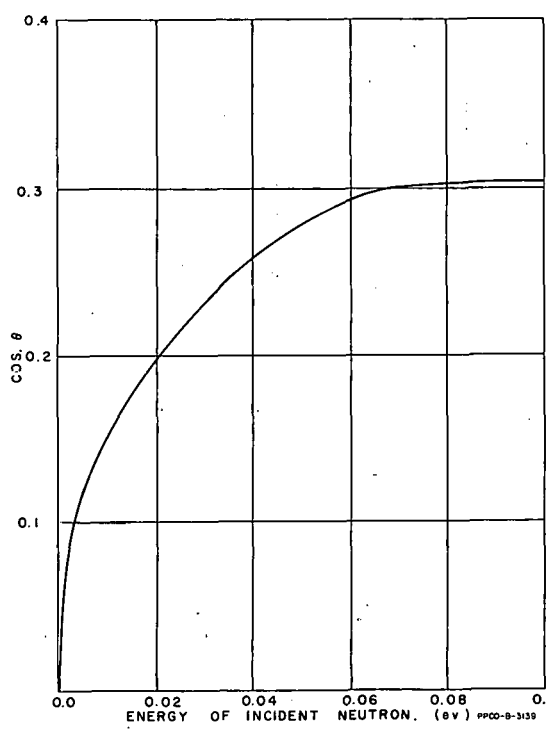

Fig. 40 Variation of the average cosine of the scattering angle with incident neutron energy for neutrons scattered by CH_4.

1.3 Average Values for Cosθ and Energy Transfer in CH_4 (G. W. Griffing, L. Gannon)

Results obtained by the K. N. method can be used readily to calculate averages such as

$$\overline{\cos\theta}\,(E_o) = \frac{\iint \cos\theta \, \frac{d^2\sigma}{d\Omega d\epsilon} \, d\epsilon d\Omega}{\sigma(E_o)}$$

$$\bar{\epsilon}\,(\theta, E_o) = \frac{\int \epsilon \, \frac{d^2\sigma}{d\Omega d\epsilon} \, d\epsilon}{\frac{d\sigma}{d\Omega}\,(\theta, E_o)}$$

$$\bar{\epsilon}\,(E_o) = \frac{\int \bar{\epsilon}\,(\theta, E_o) \, \frac{d\sigma}{d\Omega} \, d\Omega}{\sigma(E_o)}$$

Here ϵ denotes the energy transfer to the neutron.

Fig. 40 shows $\overline{\cos\theta}\,(E_o)$ plotted as a function of impact

energy, E_o. The asymptotic value of 0.3 is higher than the value ~0.2 computed using $\overline{\cos\theta} = 2/3A$ with A equal to the mass tensor value of 3.2 for the hydrogen atom. This reflects the fact that the 2/3A formula takes no account of thermal motions, or of molecular structure.

Fig. 41 shows the average energy transfer $\overline{\epsilon}(\theta, E_o)$ as a function of θ for various E_o. Positive $\overline{\epsilon}$ means the neutron gains energy on the average, negative that it loses.

Of perhaps greater interest is the mean energy transfer $\overline{\epsilon}(E_o)$. This function is plotted against E_o in Fig. 42. Curiously enough the curve consists of two straight lines for positive and negative ϵ, respectively, the curves meeting at 0.042 ev where $\overline{\epsilon} = 0$. von Dardel [34] has shown that an approximate expression for a monatomic gas of mass M which is valid when

$$E_o \gg \frac{M}{m} kT$$

is

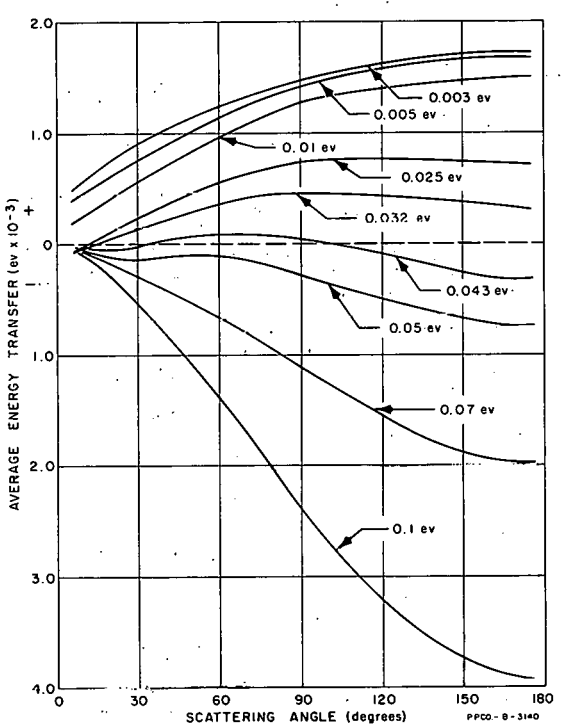

Fig. 41 Average energy transfer, $\overline{\epsilon}(\theta, E_o)$, as a function of the scattering angle for neutrons scattered by CH_4. Positive values indicate that the neutron has gained energy upon scattering, and negative values that the neutron has lost energy.

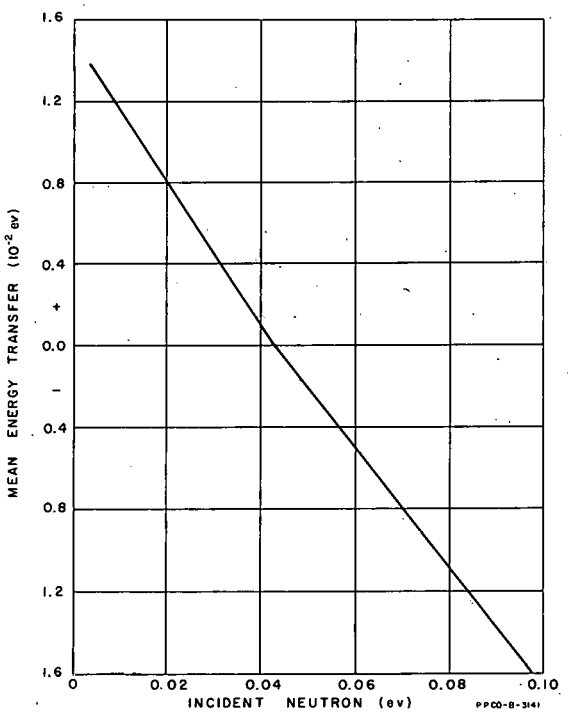

Fig. 42 Mean energy transfer $\overline{\epsilon}(E_o)$ per collision as a function of the incident neutron energy for neutrons scattered by CH_4.

$$\bar{\epsilon}\,(E_o) = \frac{1}{\left(\frac{M}{m} + 1\right)^2}\left[2\,\frac{M}{m}\,E_o - \left(4\,\frac{M}{m} - 1\right)kT - \frac{m}{M}\frac{(kT)^2}{E_o}\right]$$

at $E_o = 0.1$ and $kT = 0.0255$ ev, this equation predicts $\bar{\epsilon} = -0.019$ ev when m/M has the mass tensor value of 1/3.2 for the hydrogen atoms in CH_4. The calculated result for this energy is $\bar{\epsilon}\,(E_o) = -0.016$ ev. This equation predicts $\bar{\epsilon}\,(E_o) = 0$ at $E_o = 0.049$ ev, while the curve in Fig. 42 gives 0.042 ev. However, the conditions for the validity of von Dardel's equation begin to break down at such a low E_o, so this good agreement may be fortuitous.

2. IBM-650 PROGRAM DEVELOPMENT

2.1 IBM-650 Fortran Editor Program (G. A. Cazier)

The IBM-650 FORTRAN, a language closely resembling the language of mathematics, is designed primarily for scientific and engineering computations. One of the main drawbacks to such a language is the necessity for strict adherence to the clerical rules for constructing the mathematical statements.

To meet this problem a program entitled "650 Fortran Editor" was developed to make extensive checks on the correctness of input statements. However, the editor program that was available made use of intermediate access storage and an on-line 407 printer. Since the MTR machine configuration does not include these extras, some extensive modifications were made in the existing program to meet its requirements. With these modifications made, a "650 Fortran Editor" program that operates on a machine without core storage or an on-line printer is now available.

The use of the editor on Fortran statements prior to compilation has proved to be a savings in machine time and an aid in program debugging.

2.2 Sandwich Code (W. B. Lewis, L. Trego)

An analytical solution for a two-region, two-group treatment of an infinite one-dimensional configuration has been programmed for the IBM-650. This has particular application to the problems of nuclear safety in shipping and vault storage. The program is so indexed that a large number of parameters can be varied in a single program.

In essence, the code considers a fuel region of specified thickness (infinite extent in the other two dimensions), having specified nuclear parameters; it determines the thickness of a cadmium-moderator-cadmium sandwich that must be used to separate alternate slabs of fuel for a specified value of k_{eff}. The number of slabs so assembled is assumed to be infinite.

V. PUBLICATIONS OF MTR-ETR TECHNICAL BRANCHES

1. IDO REPORTS ISSUED

IDO-16563, ETR Cycle 18 Thermal and Fast Neutron Flux Measurements, by C. H. Hogg, L. D. Weber

IDO-16600, Coordinates for Semi-Rigid Molecules, by H. L. McMurry

IDO-16608, Line Voltage and Noise Monitor, by T. J. Boland

IDO-16620, MTR-ETR Technical Branches Quarterly Report - Period Ending December 31, 1959

IDO-16666, Proposal for an Advanced Engineering Test Reactor - ETR II, by D. R. deBoisblanc, et al.

2. PAPERS PRESENTED AT MEETINGS

2.1 Paper presented at the Northwest Computing Association Meeting, Pullman (April, 1960)

L. A. Schmittroth, Partial Differential Equations and Input/Output Buffering

2.2 Paper presented at the American Physical Society Meeting, Washington, D. C. (April, 1960)

M. S. Moore*, C. W. Reich, Anomalous Parameters of the 0.2 ev Resonance in U^{233} Slow Neutron Induced Fission

2.3 Paper presented at the Symposium on Total-Absorption Gamma-Ray Spectrometry, Gatlinburg (May, 1960)

R. L. Heath, Data Processing Techniques for Routine Application of Gamma-Ray Scintillation Spectrometry

2.4 Paper presented at the American Nuclear Society Summer Meeting, Chicago (June, 1960)

R. G. Nisle, An Integral Method for Identifying Neutron Flux Spectra

2.5 Papers presented at the Gordon Conference on Nuclear Chemistry, New Hampshire (June, 1960)

* Speaker

R. B. Regier, Mass Yields at Low Energy Resonances

R. G. Fluharty*, M. S. Moore, A Discussion of the Resonance Parameters of the Fissionable Isotopes

3. JOURNAL PUBLICATIONS

3.1 S. H. Vegors, R. L. Heath, "Isomeric Level in Pb-205 Formed in the Decay of Bi-205," Phys. Rev. 118 (April, 1960), p 547

3.2 M. S. Moore, L. G. Miller, O. D. Simpson, "Slow Neutron Total and Fission Cross Sections of U^{233}," Phys. Rev. 118 (May, 1960), p 714

3.3 M. S. Moore, C. W. Reich, "Multilevel Analysis of the Slow Neutron Cross Sections of U^{233}," Phys. Rev. 118 (May, 1960), p 718

3.4 R. L. Heath, C. W. Reich, D. G. Proctor, "Decay of 45-Day Fe-59," Phys. Rev. 118 (May, 1960), p 1082

* Speaker

VI. REFERENCES

1. ETRC Staff, "ETR Cycle 26 Fuel Loading with 400-Gram Fuel Elements," Quarterly Progress Report for MTR-ETR Technical Branches - Fourth Quarter 1959, IDO-16620 (1960), p 3

2. B. L. Hanson, "Comparison of the Reactivity Equivalence of Boron Contained in Plastic Tape and Boric Acid Solution," Quarterly Progress Report for MTR-ETR Technical Branches - Third Quarter 1958, IDO-16505 (1958), p 20

3. E. E. Burdick and R. A. Grimesey, "Comparison of ETRC Calculation with Measurements," Quarterly Progress Report for MTR-ETR Technical Branches - Third Quarter 1959, IDO-16580 (1960), p 48

4. W. R. Cadwell, "PDQ-3: A Program for the Solution of the Neutron-Diffusion Equations in Two Dimensions on the IBM-704," WAPD-TM-179 (1960)

5. R. L. Hellens, R. W. Long, and B. H. Mount, "Multigroup Fourier Transform Calculation-Description of MUFT-III Code," WAPD-TM-4 (1956)

6. D. R. Metcalf and G. A. Cazier, "Double P-1 Spherical Harmonics Approximation in Slab Geometry," IDO-16572 (1960)

7. J. Weil and P. Cabral, "P-3 Flux Distribution," IBM File No. 8.2.014

8. W. C. Francis and S. E. Craig, "Progress Report on Fuel Element Development and Associated Projects," IDO-16574 (1960)

9. R. G. Nisle, "Calculation of Isotope Production by the Cyclic Irradiation of Thorium," IDO-16504 (1959)

10. C. H. Hogg and L. D. Weber, "ETR Fast Neutron Flux Measurements," IDO-16535 (1960)

11. H. Palevsky, et al., "Direct Measurement of the Energy Variation of η for U^{233}, U^{235} and Pu^{239}," J. Nuclear Energy 3 (1956) p 177

12. J. E. Sanders, H. M. Skarsgard, and C. J. Kenward, "The Energy Dependence of the Fission Neutron Yield Per Neutron Absorbed in U^{233} over the Range 0.025 - 2.2 ev," J. Nuclear Energy 5 (1957) p 186

13. M. S. Moore, L. G. Miller, and O. D. Simpson, "Slow Neutron Total and Fission Cross Sections of U^{233}," The Phys. Rev. 118 (May 1, 1960), pp 714-17

14. M. S. Moore and C. W. Reich, "Multilevel Analysis of the Slow Neutron Cross Sections of U^{233}," The Phys. Rev. 118 (May 1, 1960), pp 718-24

15. R. L. Tromp, "Beryllium Gases Experiment," MTR-ETR Technical Branches Quarterly Report, Period Ending March 31, 1960, IDO-16633 (1960), p 19

16. B. Keisch, "Yield Ratios of Isomeric Pairs by Neutron Activation," MTR-ETR Technical Branches Quarterly Report, Period Ending December 31, 1959, IDO-16620 (1960), p 32

17. V. L. Sailor, "Spins Associated with Slow Neutron Resonances," Phys. Rev. 104 (1956), p 736

18. D. J. Hughes and R. B. Schwartz, "Neutron Cross Sections," BNL-325 2nd ed. (July 1, 1958)

19. R. L. Macklin and H. S. Pomerance, "Resonance Capture Integrals," Proc. First Intern. Conf. Peaceful Uses of Atomic Energy, Geneva 5, (1955), p 96

20. J. S. Eldridge and W. S. Lyon, "Radiations From Pm^{148}," Analytical Chemistry Division Annual Progress Report for Period Ending December 31, 1959, ORNL-2866 (1960), p 42

21. Bhattacherjee, Sahai, Baba, "Decay of Pm^{148}," Nuclear Physics, 12 (1959), pp 356-70

22. D. Strominger, J. M. Hollander, and G. T. Seaborg, "Table of Isotopes," Rev. Mod. Phys. 30 (1958), p 728

23. R. P. Schuman and J. R. Berreth, "Pile Activation Cross Section of the Pm^{148} Isomers," MTR-ETR Technical Branches Quarterly Report, Period Ending March 31, 1960, IDO-16633 (1960), p 24

24. P. A. Egelstaff, et al., Transactions of the Amer. Nuc. Soc. 3 (1960), pp 163-65

25. E. Melkonian, Phys. Rev. 76 (1949), p 1750

26. N. Z. Alcock and D. G. Hurst, Phys. Rev. 83 (1951), p 1100

27. R. G. Sachs and E. Teller, Phys. Rev. 60 (1941), p 18

28. P. A. Egelstaff, Private Communication

29. J. E. Cline and R. L. Heath, "The Decay of 15 Day Eu^{156}," Quarterly Progress Report for MTR-ETR Technical Branches - Fourth Quarter 1959, IDO-16620 (1960), p 39

30. G. T. Ewan, R. L. Graham, and J. S. Geiger, The Bull. Am. Phys. Soc. Ser II, 5 (1960), p 21

31. A. C. Zemach and R. J. Glauber, Phys. Rev. 101 (1956), pp 118-29

32. T. J. Krieger and M. S. Nelkin, Phys. Rev. 106 (1957), p 290

33. H. L. McMurry, "Scattering of Neutrons by Gaseous Molecules," IDO-16592 (March, 1960)

34. G. F. Von Dardel, Phys. Rev. 94, p 1274

Addendum to IDO-16648

The report referred to in the second paragraph, page 28 of IDO-16648 is:

W. F. Zelezny, "Metal-Water Reactions: Rates of Reaction of Aluminum and Aluminum-Uranium Alloys with Water Vapor at Elevated Temperatures", IDO-16629 (November 25, 1960).

PHILLIPS
PETROLEUM
COMPANY

PHILLIPS 66

ATOMIC ENERGY DIVISION